

# Accelerated NMR Spectroscopy: Merge Optimization with Deep Learning

Zi Wang<sup>1</sup>, Di Guo<sup>2</sup>, Yihui Huang<sup>1</sup>, Zhangren Tu<sup>2</sup>, Vladislav Orekhov<sup>3</sup>, Xiaobo Qu<sup>1\*</sup>

**Abstract:** Multi-dimensional NMR spectroscopy is an invaluable biophysical tool in studies of structure, interactions, and dynamics of large molecules like proteins and nuclear acids. Non-uniform sampling is a powerful approach for shortening measurement time and increasing spectra resolution. Several methods have been established for spectra reconstruction from the undersampled data, typical approaches include model-based optimization and data-driven deep learning. The former is well theoretically grounded and provides high-quality spectra, while the latter has a huge advantage in reconstruction time potential and push further limits of spectra quality and analysis. Combining the merits of the two, we propose a model-inspired deep learning, for reliable, high-quality, and ultra-fast spectra reconstruction, exemplified by multi-dimensional spectra of several representative proteins. We demonstrate that the proposed network needs very few parameters, and shows very high robustness in respect to dissimilarity of the training and target data in the spectra size, type, and sampling level. This work can be considered as a proof-of-concept of merging optimization with deep learning in NMR spectroscopy.

NMR spectroscopy serves as an indispensable biophysical tool in modern chemistry, biology, and life science<sup>1-4,37</sup>. Since the duration of an NMR experiment is proportional to the number of measured data points and increases rapidly with the dimensionality and spectral resolution, accelerating the measurement time by using the non-uniform sampling (NUS) approach<sup>5,6</sup> becomes widely accepted practice. Over the past two decades, a number of methods have been successfully used in the NMR field to reconstruct high-quality spectra from NUS data. The two distinct strategies are model- or prior-based optimization<sup>7-19</sup> and data-driven deep learning<sup>20-24</sup>. The former has the explicit modeling and specific priors with insights from NMR spectroscopy, while the latter relies on low-complexity algorithms to greatly reduce the reconstruction time.

For model-based optimization methods, similarly, they rely on the prior knowledge or assumptions, to compensate for the lack of information introduced by the NUS scheme. A range of modern approaches include the maximum entropy<sup>6</sup>, spectral lineshape estimation<sup>7</sup>, tensor structures<sup>5</sup>, compressed sensing (CS)<sup>8-13</sup>, and low-rank Hankel matrices and tensors<sup>14-19</sup>. Among them, CS introduces the reasonable assumption of NMR spectral sparsity, and utilizes the explicit structure and simple iterative algorithms to reconstruct NMR spectra. It can be regarded as an effective self-learning method by iterating on a single input. Nevertheless, the sparseness prior of the CS has limitations on broad peaks<sup>14</sup> and the computations are lengthy. Moreover, with the decrease of the NUS densities and the increase of the spectra size, the computational time for

reconstructing high-quality spectra increases significantly, which drives development of new techniques.

Data-driven deep learning (DL) is a representative artificial intelligence technique utilizing neural networks<sup>25</sup>. Due to the low-complexity non-iterative algorithm and massive parallelization with graphic processing units (GPUs), a trained network can reconstruct a high-quality spectrum<sup>20-24</sup> very fast. However, the existing NMR DL networks contain too many adjustable parameters and are over-parametrized. Consequently, they require very large pool of data for training, an excessively large operative memory, and suffer from lack of robustness and explainability<sup>23</sup>. Hence, the question remains, can a deep network achieve even better performance in spectra quality and computational efficiency while having an understandable architecture for human NMR experts?

Now, we feel strongly that, so far independent development of optimization and deep learning methods approached to the merging stage, and it is a trend of the future technology development. Effectiveness of fusion between the optimization and deep learning has been recently successfully demonstrated in signal processing and other areas<sup>26-30</sup>, which encourages us to provide a clear guidance for merging the optimization and deep learning in NMR.

Herein, we introduce a Model-inspired Deep learning framework, called MoDern. Our design of architecture starts from the sparse prior knowledge and adopts the main idea from the classic CS algorithm: iterative soft-thresholding (IST)<sup>10,13</sup>.

Let  $\mathbf{r}$  be the complete NMR time-domain signal, called free induction decay (FID), and the forward Fourier transform  $\mathbf{F}$  converts it into a NMR spectrum  $\mathbf{x} = \mathbf{Fr}$ . In NMR spectroscopy, CS model states that the sparsest solution can be always found by the  $\ell_1$  norm optimization<sup>10,11,31</sup>. This task can be efficiently solved by the IST algorithm, and its  $k^{th}$  ( $k = 1, \dots, K$ ) iteration process can be written as follows<sup>10,13</sup>:

$$(\text{Data Consistency}) \quad \mathbf{d}_k = \mathbf{x}_{k-1} + \mathbf{FU}^T (\mathbf{y} - \mathbf{UF}^H \mathbf{x}_{k-1}), \quad (1a)$$

$$(\text{Soft-thresholding}) \quad \mathbf{x}_k = S(\mathbf{d}_k, \theta), \quad (1b)$$

where  $\mathbf{y}$  is the FID signal undersampled by operator  $\mathbf{U}$ ,  $\mathbf{F}^H$  is the inverse Fourier transform,  $\mathbf{d}$  is the spectrum after data consistency, the superscript  $T$  is the transpose operator,  $\theta$  is the threshold, and  $S(x, \theta) = \max\{|x| - \theta, 0\} \cdot x/|x|$  is the soft-thresholding operator. Initialized with  $\mathbf{x}_0 = \mathbf{FU}^T \mathbf{y}$ , CS reconstructs the spectrum by alternating the data consistency and the soft-thresholding.

Once the overall number of iterations is fixed, the data flow can be viewed as an unfolded deep learning network, as shown in Figure 1. Same to Eq. (1a), the spectrum is forced to maintain the data consistency to the sampled signal. Since the proper

<sup>1</sup>Department of Electronic Science, National Institute for Data Science in Health and Medicine, Xiamen University, Xiamen 361005, China. <sup>2</sup>School of Computer and Information Engineering, Xiamen University of Technology, Xiamen 361024, China. <sup>3</sup>Department of Chemistry and Molecular Biology, University of Gothenburg, Box 465, Gothenburg 40530, Sweden.

Correspondence should be addressed to Xiaobo Qu (quxiaobo@xmu.edu.cn).

choice of thresholds is still of great demand and challenging, thus, instead of Eq. (1b), we use a learnable network  $LS$  which can change thresholds with the characteristics of the input data, for adaptive soft-thresholding. The single network  $LS$  is composed of convolutional layers, fully-connected layers, and a soft-thresholding (See in the Supplement S1.2 for details). Our experiments demonstrate the effectiveness of this scheme (See in the Supplement S1.4 for details). With the increase of iterations, artifacts are gradually removed, and finally a high-quality reconstructed spectrum can be obtained.

Given the success of training neural networks using solely synthetic data with the exponential functions<sup>20,22</sup>, we also

employ this scheme to train our network to learn the best internal parameters  $\hat{\Theta}$  and an optimal mapping  $f(\mathbf{y}, \hat{\Theta})$  by minimizing the mean square error between outputs of the learnable adaptive soft-thresholding and fully sampled spectra. For a well-trained network, the spectrum  $\bar{\mathbf{x}}$  can be reconstructed reliably and fast from an undersampled signal  $\mathbf{y}$  via  $f(\mathbf{y}, \hat{\Theta})$ . Notably, the self-learning CS approach often needs lots of iterations, however, the trained deep learning network with the fixed number of iterations is a simple forward model, which greatly shorten the reconstruction time.

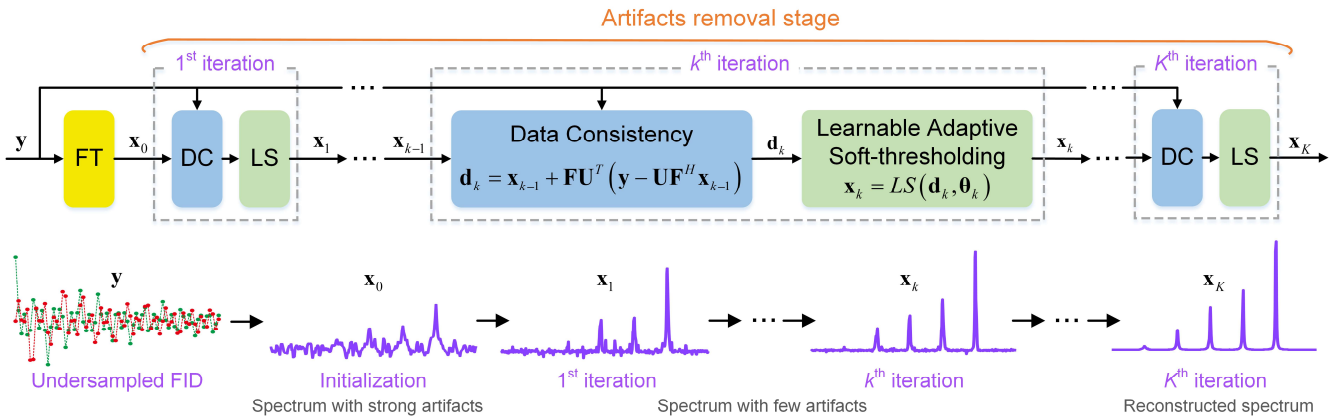


**Figure 1.** MoDern: The proposed Model-inspired Deep Learning framework for NMR spectra reconstruction. The recursive MoDern framework that alternates between the data consistency (DC), which is same to Eq. (1a), and the learnable adaptive soft-thresholding (LS) inspired by Eq. (1b). With the increase of the iteration, artifacts are gradually removed, the spectrum tends to be “sparse”, and finally a high-quality reconstructed spectrum can be obtained. Note: “FT” is the Fourier transform. A data consistency followed by a learnable adaptive soft-thresholding constitutes an iteration.

MoDern is inspired by the CS, but go beyond it due to the learning ability of the deep neural network. For example, we solve the limitation of CS on broad peaks. Figure 2 shows a comparison between a synthetic fully sampled reference spectrum and its NUS reconstructions obtained using CS<sup>10</sup> and MoDern. The spectrum contains five peaks with different line widths. It can be observed that while the narrowest Peak 5 is successfully recovered, the other four peaks have visible distortions exacerbated as the peaks get broader (Figure 2b). Meanwhile, MoDern reconstructs all five peaks faithfully (Figure 2c). Figure 2d and 2e show that, for the NUS density in the range 10%~20%, MoDern has higher peak intensity correlations to the reference spectrum than CS in recovering three broadest peaks, and results are comparable for the remaining peaks. Similar results have been observed on a 2D <sup>1</sup>H-<sup>15</sup>N HSQC spectrum of the cytosolic domain of CD79b in Figure 3 (See in the Supplement S2 for details). Thus, we can conclude that, MoDern produces at least as good spectra reconstruction as CS and often outperforms it for broadest and weakest peaks, which indicate high effective sensitivity<sup>32</sup> of MoDern.

By abandoning a large number of redundant convolution layers, which is often used in the data-driven deep learning<sup>20,22</sup>, number of the network parameters of MoDern is ca 9% of that needed for the state-of-the-art DLNMR<sup>20</sup> (Figure 4a), resulting in a significant reduction in both training and reconstruction time (Figure 4b) without loss of spectral reconstruction quality (See in the Supplement S4 for details).

Since the integration of optimization alleviates the network’s dependence on the training dataset, MoDern is very flexible and can overcome the mismatch between training and real datasets, e.g. difference in spectra size, type, and NUS density, to work effectively in a wide range of scenarios without re-training. Thus, Figure 4c and 4d show that MoDern maintains the high-quality and significantly better than DLNMR reconstruction performance when the NUS density of spectra significantly deviates from the level used in the training (See in the Supplement S3 for details).

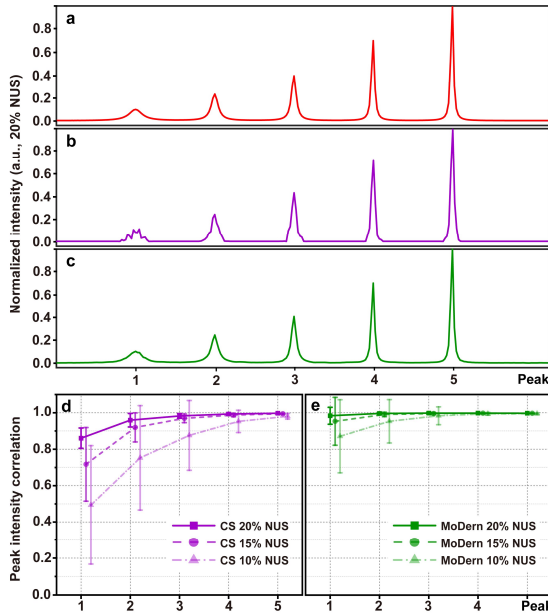


**Figure 2.** Reconstruction of the synthetic spectrum with five peaks. (a) The fully sampled spectrum. (b) and (c) are the reconstructed spectra using CS and MoDern from 20% data, respectively. (d) and (e) are peak intensity correlations between fully sampled spectrum and reconstructed spectrum using CS and MoDern under different NUS densities, respectively. Note: The solid, dashed, and dot-dashed lines in (d) and (e) connect results of the reconstructions using 20%, 15% and 10% NUS, respectively. The average and standard deviations of correlations in (d) and (e) are computed over 100 NUS trials (different sampling masks under the same NUS densities).

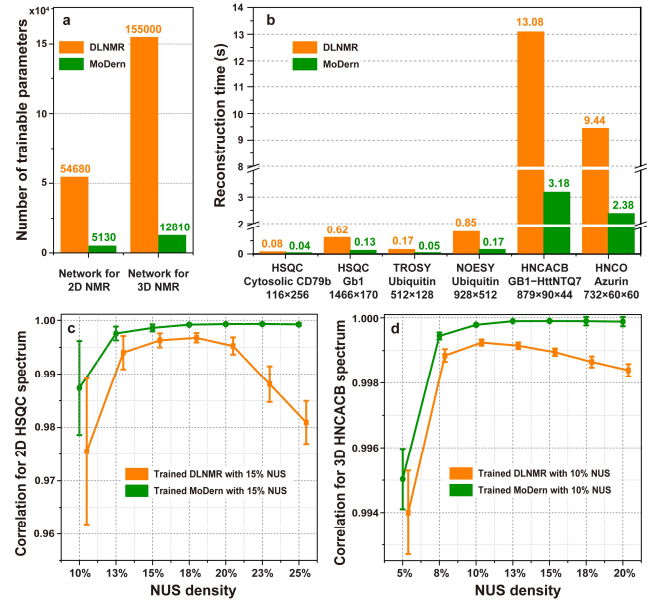


**Figure 3.** Comparison between DLNMR and MoDern in 2D and 3D spectra reconstruction. (a) is the number of trainable parameters of two networks. (b) is the reconstruction time of two networks. (c) Peak intensity correlations of DLNMR and MoDern trained using 15% NUS density dataset respectively, to reconstruct 2D 1H-15N HSQC spectrum of the cytosolic domain of CD79b, under a series of NUS densities ranging from 10% to 25%. (d) Peak intensity correlations of DLNMR and MoDern trained using 10% NUS density dataset respectively, to reconstruct 3D HNCACB spectrum of GB1-HttNTQ7, under a series of NUS densities ranging from 5% to 20%. Note: Below each bar of (b), the spectrum type, corresponding protein, and spectrum size are listed. For 2D (3D) spectra, the size of the directly detected dimension is followed by the size(s) of the indirect dimension(s). The peak intensity correlations of DLNMR (orange line) are shifted horizontally for clear display but the values unchanged. The average and standard deviations of correlations in (c) and (d) are computed over 100 and 50 NUS trials, respectively.

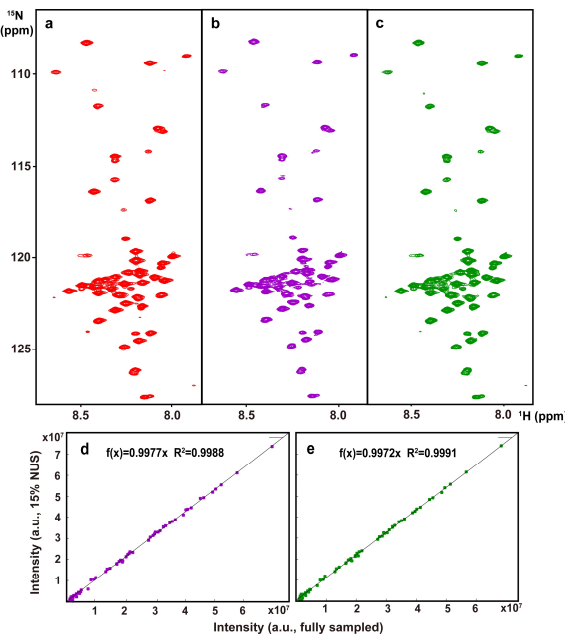


**Figure 3.** Reconstruction of 2D  $^1\text{H}$ - $^{15}\text{N}$  HSQC spectrum of the cytosolic domain of CD79b. (a) The fully sampled spectrum. (b) and (c) are the reconstructed spectra using CS and MoDern from 15% data, respectively. (d) and (e) are peak intensity correlations between fully sampled spectrum and reconstructed spectrum using CS and MoDern, respectively. Note: The  $R^2$  denotes the square of Pearson correlation coefficient. The closer the value of  $R^2$  gets to 1, the stronger the correlation between the fully sampled spectra and the reconstructed spectra is.

To demonstrate the reliability and high-quality of MoDern, we perform spectrum reconstructions of several fully sampled two- and three-dimensional experiments of representative proteins. Figure 5a shows that MoDern can faithfully reconstruct the high dynamic range 2D NOESY spectrum of human ubiquitin with many weak peaks using 40% NUS data. We observe 0.9931 correlation (vs the fully sampled spectrum) for the intensities of the weak peaks (<4% of the highest diagonal peak intensity), which is comparable to CS<sup>10</sup> and much better than DLNMR<sup>20</sup> (See in the Supplement S2.2 for details). The peak intensity correlations over 0.99 are also observed for three other 2D spectra with moderate dynamic range (See in the Supplement S2.2 for details). MoDern also shows its great potential in fast high-quality reconstruction of 3D spectra, exemplified by 3D HNCACB experiment for GB1-HttNTQ7 (Figure 5c). The peak intensity correlation reaches 0.99 even at 20 times acceleration, i.e. 5% NUS. The excellent performance also indicates on another 3D HNCO for Azurin, while its peak intensity correlation over 0.99 (See in the Supplement S2.3 for details).

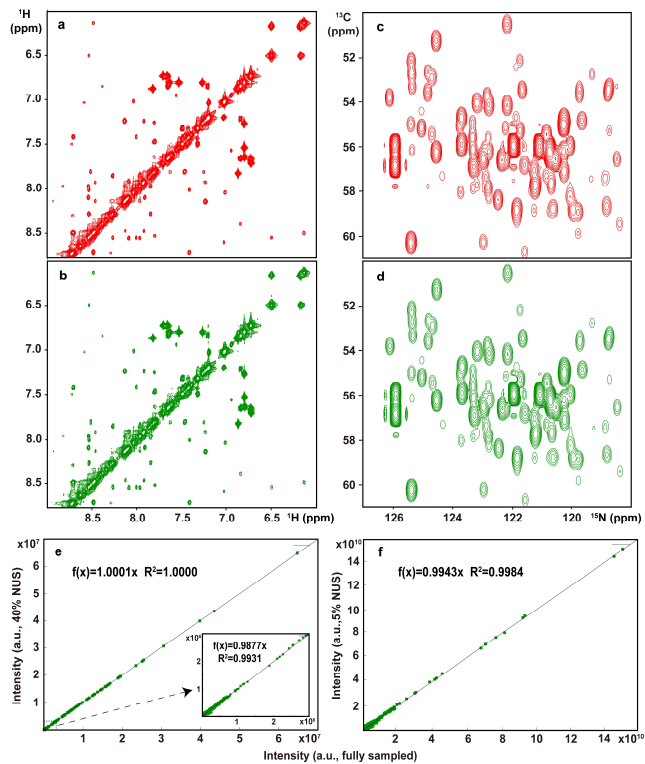


**Figure 5.** 2D and 3D spectra reconstruction. (a-b) The fully sampled 2D <sup>1</sup>H NOESY spectrum of human ubiquitin and the reconstructed spectrum using MoDern from 40% data. (c-d) The sub-regions of <sup>13</sup>C-<sup>15</sup>N projection from the fully sampled 3D HNCACB spectrum of GB1-HttNTQ7 and the reconstructed spectrum using MoDern from 5% data. (e-f) Peak intensity correlations between MoDern reconstructions and the fully sampled 2D NOESY spectrum and 3D HNCACB spectrum, respectively. The inset of (e) shows the peak intensity correlation of weak peaks (<4% of the highest diagonal peak intensity) obtain by MoDern.

In summary, we propose a deep learning framework inspired by the CS model, called MoDern, as a reliable, versatile, and ultra-fast technique for obtaining high-quality spectra from NUS data. As such, MoDern will benefit numerous NMR applications in structural and medical biology. Furthermore, by combining the power of data-driven deep learning with the model-based optimization, the method provides a rarely available understanding of the complex mapping of the deep neural network. This opens an avenue for theoretical analysis of this neural network to explore its underlying mechanisms, and also be valuable to other biomedical imaging tools<sup>33-36</sup>. This work is a proof-of-principle demonstration of the effectiveness of merging the model-based optimization and deep learning in biological NMR.

## References

- 1 Sounier, R. *et al.* Propagation of conformational changes during  $\mu$ -opioid receptor activation. *Nature* **524**, 375-378, (2015).
- 2 Theillet, F.-X. *et al.* Structural disorder of monomeric  $\alpha$ -synuclein persists in mammalian cells. *Nature* **530**, 45-50, (2016).
- 3 Barraud, P. *et al.* Time-resolved NMR monitoring of tRNA maturation. *Nat. Commun.* **10**, 3373, (2019).
- 4 Inomata, K. *et al.* High-resolution multi-dimensional NMR spectroscopy of proteins in human cells. *Nature* **458**, 106-109, (2009).
- 5 Jaravine, V., Ibraghimov, I. & Yu Orekhov, V. Removal of a time barrier for high-resolution multidimensional NMR spectroscopy. *Nat. Meth.* **3**, 605-607, (2006).
- 6 Mobli, M. & Hoch, J. C. Nonuniform sampling and non-Fourier signal processing methods in multidimensional NMR. *Prog. Nucl. Magn. Reson. Spectrosc.* **83**, 21-41, (2014).
- 7 Ying, J., Delaglio, F., Torchia, D. A. & Bax, A. Sparse multidimensional iterative lineshape-enhanced (SMILE) reconstruction of both non-uniformly sampled and conventional NMR data. *J. Biomol. NMR* **68**, 101-118, (2017).
- 8 Qu, X., Cao, X., Guo, D. & Chen, Z. Reconstruction of self-sparse 2D NMR spectra from undersampled data in indirect dimension. in *International Society for Magnetic Resonance in Medicine 19th Scientific Meeting (ISMRM)*, 3371, (2010).
- 9 Qu, X., Guo, D., Cao, X., Cai, S. & Chen, Z. Reconstruction of self-sparse 2D NMR spectra from undersampled data in indirect dimension. *Sensors* **11**, 8888-8909 (2011).
- 10 Kazimierczuk, K. & Orekhov, V. Y. Accelerated NMR spectroscopy by using compressed sensing. *Angew. Chem. Int. Ed.* **50**, 5556-5559, (2011).
- 11 Holland, D. J., Bostock, M. J., Gladden, L. F. & Nietlispach, D. Fast Multidimensional NMR spectroscopy using compressed sensing. *Angew. Chem. Int. Ed.* **50**, 6548-6551, (2011).
- 12 Shrot, Y. & Frydman, L. Compressed sensing and the reconstruction of ultrafast 2D NMR data: Principles and biomolecular applications. *J. Magn. Reson.* **209**, 352-358, (2011).
- 13 Hyberts, S. G., Milbradt, A. G., Wagner, A. B., Arthanari, H. & Wagner, G. Application of iterative soft thresholding for fast reconstruction of NMR data non-uniformly sampled with multidimensional Poisson Gap scheduling. *J. Biomolecular NMR* **52**, 315-327, (2012).
- 14 Qu, X., Mayzel, M., Cai, J.-F., Chen, Z. & Orekhov, V. Accelerated NMR spectroscopy with low-rank reconstruction. *Angew. Chem. Int. Ed.* **54**, 852-854, (2015).
- 15 Ying, J. *et al.* Vandermonde factorization of Hankel matrix for complex exponential signal recovery—Application in fast NMR spectroscopy. *IEEE Trans. Signal Process.* **66**, 5520-5533, (2018).
- 16 Lu, H. *et al.* Low rank enhanced matrix recovery of hybrid time and frequency data in fast magnetic resonance spectroscopy. *IEEE Trans. Biomed. Eng.* **65**, 809-820, (2018).
- 17 Guo, D., Lu, H. & Qu, X. A fast low rank Hankel matrix factorization reconstruction method for non-uniformly sampled magnetic resonance spectroscopy. *IEEE Access* **5**, 16033-16039, (2017).
- 18 Ying, J. *et al.* Hankel matrix nuclear norm regularized tensor completion for N-dimensional exponential signals. *IEEE Trans. Signal Process.* **65**, 3702-3717, (2017).
- 19 Qiu, T., Wang, Z., Liu, H., Guo, D. & Qu, X. Review and prospect: NMR spectroscopy denoising and reconstruction with low-rank Hankel matrices and tensors. *Magn. Reson. Chem.*, doi:10.1002/mrc.5082 (2020).
- 20 Qu, X. *et al.* Accelerated nuclear magnetic resonance spectroscopy with deep learning. *Angew. Chem. Int. Ed.* **59**, 10297-10300, (2020).
- 21 Hansen, D. F. Using deep neural networks to reconstruct non-uniformly sampled NMR spectra. *J. Biomol. NMR* **73**, 577-585, (2019).
- 22 Huang, Y., Zhao, J., Wang, Z., Guo, D. & Qu, X. Exponential signal reconstruction with deep Hankel matrix factorization. *arXiv:2007.06246*, (2020).
- 23 Chen, D., Wang, Z., Guo, D., Orekhov, V. & Qu, X. Review and prospect: Deep learning in nuclear magnetic resonance spectroscopy. *Chem. Eur. J.* **26**, 10391-10401, (2020).
- 24 Karunaniy, G. H., Flemming. FID-Net: A versatile deep neural network architecture for NMR spectral reconstruction and virtual decoupling. *ChemRxiv:13295888*, (2020).
- 25 LeCun, Y., Bengio, Y. & Hinton, G. Deep learning. *Nature* **521**, 436-444, (2015).
- 26 Zhang, J. & Ghanem, B. ISTA-Net: Interpretable optimization-inspired deep network for image compressive sensing. in *2018 IEEE/CVF Conference on Computer Vision and Pattern Recognition (CVPR)*, 1828-1837, (2018).
- 27 Yang, Y., Sun, J., H, L. I. & Xu, Z. ADMM-CSNet: A deep learning approach for image compressive sensing. *IEEE Trans. Pattern Anal.* **42**, 521-538, (2020).

28 Jacob, M., Ye, J. C., Ying, L. & Doneva, M. Computational MRI: Compressive sensing and beyond. *IEEE Signal Proc. Mag.* **37**, 21-23, (2020).

29 Liu, Y. *et al.* Projected iterative soft-thresholding algorithm for tight frames in compressed sensing magnetic resonance imaging. *IEEE Trans. Med. Imaging* **35**, 2130-2140, (2016).

30 Lu, T. *et al.* pFISTA-SENSE-ResNet for parallel MRI reconstruction. *J. Magn. Reson.* **318**, 106790, (2020).

31 Shchukina, A., Kasprzak, P., Dass, R., Nowakowski, M. & Kazimierczuk, K. Pitfalls in compressed sensing reconstruction and how to avoid them. *J. Biomol. NMR* **68**, 79-98, (2017).

32 Hyberts, S. G., Robson, S. A. & Wagner, G. Exploring signal-to-noise ratio and sensitivity in non-uniformly sampled multi-dimensional NMR spectra. *J. Biomol. NMR* **55**, 167-178, (2013).

33 Durand, A. *et al.* A machine learning approach for online automated optimization of super-resolution optical microscopy. *Nat. Commun.* **9**, 5247, (2018).

34 Zhu, B., Liu, J. Z., Cauley, S. F., Rosen, B. R. & Rosen, M. S. Image reconstruction by domain-transform manifold learning. *Nature* **555**, 487-492, (2018).

35 Wang, G., Ye, J. C. & De Man, B. Deep learning for tomographic image reconstruction. *Nat. Machine Intelligence* **2**, 737-748, (2020).

36 Wang, S. *et al.* Accelerating magnetic resonance imaging via deep learning. in *2016 IEEE 13th International Symposium on Biomedical Imaging (ISBI)*, 514-517, (2016).

37 Kotler, S. *et al.* Probing initial transient oligomerization events facilitating Huntingtin fibril nucleation at atomic resolution by relaxation-based NMR. *Proc. Natl. Acad. Sci. U. S. A.* **116**, 3562-3571, (2019).

## Acknowledgements

The authors thank Marius Clore and Samuel Kotler for providing the 3D HNCACB data; Jinfa Ying for assisting in processing and helpful discussions on the 3D HNCACB spectrum; Luke Arbogast and Frank Delaglio for providing the 2D HSQC spectrum of GB1. This work was supported in part by the National Natural Science Foundation of China (NSFC) under grants 61971361, 61871341, and U1632274, the Joint NSFC-Swedish Foundation for International Cooperation in Research and Higher Education (STINT) under grant 61811530021, the National Key R&D Program of China under grant 2017YFC0108703, the Natural Science Foundation of Fujian Province of China under grant 2018J06018, the Fundamental Research Funds for the Central Universities under grant 20720180056, the Xiamen University Nanqiang Outstanding Talents Program, the Swedish Research Council under grant 2015-04614, and the Swedish Foundation for Strategic Research under grant ITM17-0218.

## Author contributions

X. Qu and Z. Wang conceived the idea and designed the study, X. Qu supervised the project, Z. Wang and Z. Tu implemented the method and produced the results, Z. Wang drew all the figures for the manuscript and supplement. All authors were involved in the data analysis. The manuscript was drafted by Z. Wang and improved by Z. Wang, D. Guo, Y. Huang, Z. Tu, V. Orekhov, and X. Qu. X. Qu and D. Guo acquired research funds and provided all the needed resources.

## Competing interests

The authors declare no competing interests.

## Data availability

The synthetic FID data used for training will be shared at <http://csrc.xmu.edu.cn>. The 2D HSQC spectrum of Gb1 is available from nmrPipe website (<https://www.ibbr.umd.edu/nmrpipe/index.html>). The 3D HNCO spectrum of Azurin is available from MddNMR website (<http://mddnmr.spektrino.com/>). The spectra data of 2D HSQC of Cytosolic CD79b, 2D NOESY of Ubiquitin, 2D TROSY of Ubiquitin, and 3D HNCACB of GB1-HttNTQ7 are available from the corresponding author upon reasonable request.

## Code availability

Code is available from the corresponding author upon reasonable request.



# Supplement

## Accelerated NMR Spectroscopy: Merge Optimization with Deep Learning

Zi Wang,<sup>[a]</sup> Di Guo,<sup>[b]</sup> Yihui Huang,<sup>[a]</sup> Zhangren Tu,<sup>[b]</sup> Vladislav Orekhov,<sup>[c]</sup> Xiaobo Qu\*<sup>[a]</sup>

[a] Department of Electronic Science, National Institute for Data Science in Health and Medicine, Xiamen University, Xiamen 361005, China

[b] School of Computer and Information Engineering, Xiamen University of Technology, Xiamen 361024, China

[c] Department of Chemistry and Molecular Biology, University of Gothenburg, Box 465, Gothenburg 40530, Sweden

\*E-mail: [quxiaobo@xmu.edu.cn](mailto:quxiaobo@xmu.edu.cn)

## S1. Theory and methodology

### 1.1 The network architecture

In NMR spectroscopy, the typical signal sampled in the time domain  $\mathbf{r} \in \mathbb{C}^N$ , called free induction decay (FID), is commonly described as a sum of decaying complex exponents<sup>1,2</sup>:

$$r_n = \sum_{j=1}^J (a_j e^{i\phi_j}) e^{-\frac{n\Delta t}{\tau_j}} e^{in\Delta f_j}, \quad n \in \{1, 2, \dots, N\}, \quad (\text{S1-1})$$

where  $\Delta t$  is the time interval,  $J$  is the number of spectral peaks,  $a_j$ ,  $f_j$ ,  $\tau_j$ , and  $\phi_j$  are the amplitude, frequency, decay time, and phase of the  $j^{\text{th}}$  spectral peak, respectively.

The NMR spectrum  $\mathbf{x} = \mathbf{F}\mathbf{r} \in \mathbb{C}^N$  can be reconstructed by solving the following compressed sensing (CS) problem<sup>3-6</sup>:

$$\min_{\mathbf{x}} \frac{1}{2} \|\mathbf{y} - \mathbf{U}\mathbf{F}^H \mathbf{x}\|_2^2 + \lambda \|\mathbf{x}\|_1, \quad (\text{S1-2})$$

where  $\mathbf{y} \in \mathbb{C}^M$  is the FID undersampled by operator  $\mathbf{U} \in \mathbb{R}^{M \times N}$ ,  $\mathbf{F}$  is the forward Fourier transform, superscript  $H$  denotes the Hermitian conjugate operator,  $\|\cdot\|_2$  represents the  $l_2$  norm,  $\|\cdot\|_1$  represents the  $l_1$  norm, and  $\lambda$  is the regularization parameter that balances the data consistency and the sparsity. Iterative soft-thresholding (IST) is an efficient algorithm to solve Eq. (S1-2), and its  $k^{\text{th}}$  iteration process can be written as follows:

$$\begin{cases} \mathbf{d}_k = \mathbf{x}_{k-1} + \mathbf{F}\mathbf{U}^T (\mathbf{y} - \mathbf{U}\mathbf{F}^H \mathbf{x}_{k-1}) \\ \mathbf{x}_k = S(\mathbf{d}_k, \theta) \end{cases}, \quad (\text{S1-3})$$

where  $k = 0, 1, 2, \dots, K$  represents the  $k^{\text{th}}$  iteration process, superscript  $T$  denotes the transpose operator,  $\theta$  is the threshold, and  $S(x, \theta) = \max\{|x| - \theta, 0\} \cdot x / |x|$  is the soft-thresholding operator.

Herein, inspired by the CS approach, then we derived the data flow of IST algorithm and design a model-inspired deep learning framework, called MoDern, whose detailed architecture is shown in Figure S1-1. The implementation of MoDern includes two stages, training stage and reconstruction stage, and both of them are

illustrated in the following.

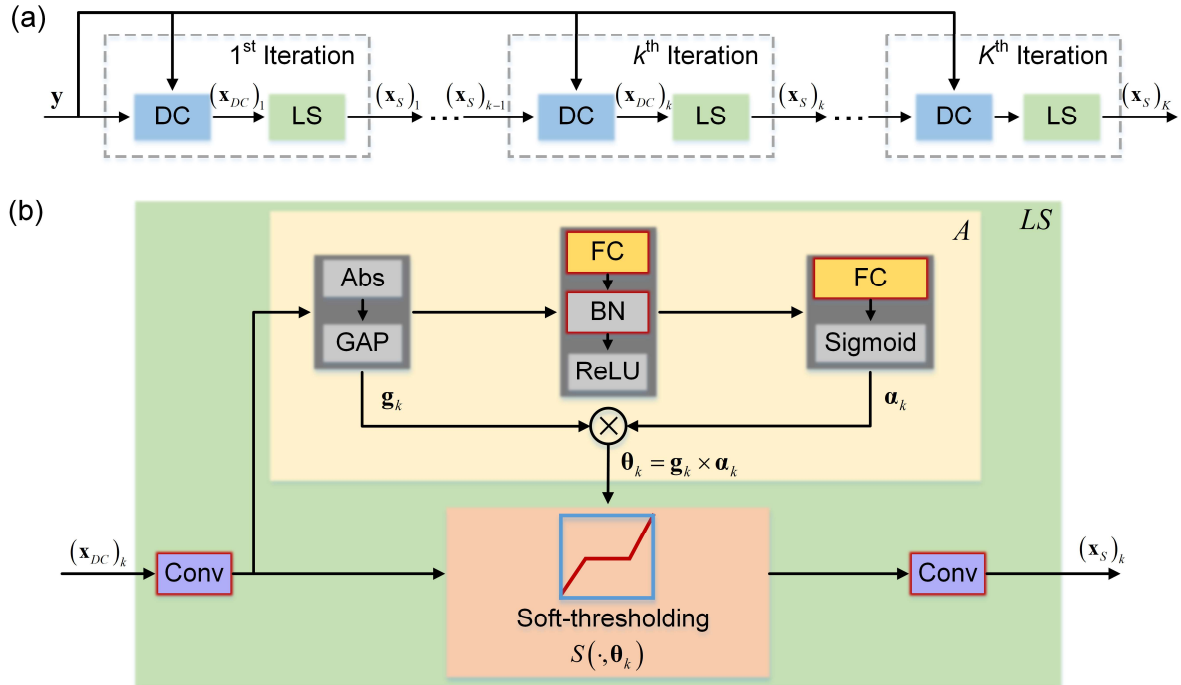


**Figure S1-1.** MoDern: The proposed Model-inspired Deep learning framework for NMR spectra reconstruction. (a) is the Unfold architecture for  $K$  iterations and it alternates between data consistency (DC) and learnable adaptive soft-thresholding (LS). (b) shows the learnable adaptive soft-thresholding block  $LS$  and threshold auto-setting sub-block  $A$  in detail. Note: in (b), the trainable parts are highlighted in red box. ‘Conv’ is the convolution layer, ‘Abs’ is the absolute operation, ‘GAP’ is the global average pooling, ‘FC’ is the fully-connected layer, ‘BN’ is the batch normalization, ‘ReLU’ and ‘Sigmoid’ are non-linear functions.

## 1.2 Training stage of the network

### 1.2.1 Generation of the training/validation datasets

Given the success of training neural networks using solely synthetic data with the exponential functions<sup>7</sup>, our network also employs this scheme to form the training dataset and validation dataset, which makes the network training not affected by the lack of realistic data.

The 40000 fully sampled synthetic FIDs are generated according to Eq. (S1-1) and their parameters are in Table S1-1. The white Gaussian noise at the level with the standard deviation of  $10^{-4}$  is added to the each synthetic FID to simulate the realistic NMR data, so that the trained network can be better applied to the reconstruction of measurements.

Let  $y$  denotes the FID undersampled by operator  $U$  following the Poisson-gap sampling scheme<sup>8</sup>,  $F$  denotes the forward Fourier transform, so 40000 undersampled FIDs  $y=Ur$  (the sampling mask is different for each of 40000 FIDs to enrich the diversity of the training dataset) and 40000 fully sampled spectra  $x=Fr$  are generated correspondingly. To eliminates the dispersion part of the spectrum, make the spectrum “sparser”,

and allows spectrum reconstruction with better fidelity and from fewer measurements, virtual echo (VE) method is used<sup>9</sup>.

Let  $q=1,2,\dots,Q$  denotes the  $q^{\text{th}}$  sampling trail, then we have  $Q=40000$  pairs of data  $(\mathbf{y}_q, \mathbf{x}_q)$ . The undersampled FID  $\mathbf{y}_q$  and the fully sampled spectrum  $\mathbf{x}_q$ , are the input and label of the network, respectively. Among the 40000 pairs of data  $(\mathbf{y}_q, \mathbf{x}_q)$ , 90% of the data (36000 pairs) is used as training dataset to train the neural network for obtaining the optimal internal parameters and mapping, and 10% of the data (4000 pairs) is used as validation dataset to adjust the hyper-parameters and evaluate the network's performance preliminarily.

**Table S1-1.** Parameters of the generated synthetic training dataset

Parameters	Minimum	Increment	Maximum
Number of peaks	1	1	10
Amplitude	0.05	continuous	1.00
Frequency	0.01	continuous	0.99
Decay time	10.00	continuous	179.20
Phase	0	continuous	$2\pi$

### 1.2.2 Data consistency block

In this block, each spectrum is forced to maintain the data consistency to the sampled signal, which can ensure reconstructed spectra are aligned to acquired data. Just like the first step of the IST algorithm (Figure S1-1(a)), after inputting the output of the last iteration, i.e. the output of the learnable adaptive soft-thresholding block  $\mathbf{x}_s$ , the spectrum becomes

$$\mathbf{x}_{DC} = \mathbf{x}_s + \mathbf{F}\mathbf{U}^T (\mathbf{y} - \mathbf{U}\mathbf{F}^H \mathbf{x}_s), \quad (S1-4)$$

where  $\mathbf{F}$  is the forward Fourier transform, superscript  $H$  denotes the Hermitian conjugate operator,  $\mathbf{x}_{DC}$  is the output of the data consistency block,  $\mathbf{U}$  is the undersampling operator. To show the function of this block more intuitively, Eq. (S1-4) can also be equivalent to

$$(\mathbf{x}_{DC})_n = \begin{cases} \mathbf{x}_s, & n \notin \Omega \\ \mathbf{y}, & n \in \Omega \end{cases}, \quad (S1-5)$$

where  $n$  is the index of FIDs and  $\Omega$  is the set of the sampled positions in FIDs. Eq. (S1-5) implies that, at the sampled positions, the points should be replaced with the original inputs  $\mathbf{y}$ , while the update of the unsampled points depends entirely on the reconstruction results of the network.

In our implementation, the initial spectrum that inputs the neural network is computed as  $\mathbf{x}_0 = \mathbf{F}\mathbf{U}^T \mathbf{y}$ . The initial input  $\mathbf{x}_0$  is with strong artifacts since those unsampled FIDs are filled with zeros on non-acquired positions.

### 1.2.3 Learnable adaptive soft-thresholding block

Soft-thresholding operation is always used to remove irrelevant artifact-related information. In conventional iterative methods<sup>3,6</sup>, the optimal value of the threshold depends on the data, i.e. number of signals and their signal dynamic range, noise level, and even position in the spectrum. Thus, in practice, a relatively safe, high threshold is applied resulting in large number of iterations and, consequently, long calculations as well as poor reconstruction of broad lines. The key advantage of our approach is the use of a neural network for defining the optimal threshold for each iteration and for each point in the spectrum. We introduce the learnable adaptive soft-thresholding blocks, which sets the optimal threshold according to the characteristics of the input, to reduce artifacts of the input spectra. The block consists of several elements, including convolution layer (Conv), absolute (Abs), global average pooling (GAP), fully-connected layer (FC), batch normalization (BN), non-linear functions (ReLU and Sigmoid), and soft-thresholding.

As shown in Figure S1-1(b), similar to IST algorithm, we directly use the soft-thresholding operation to remove artifacts, and discard a lot of redundant convolution layers<sup>10</sup>, which makes the network architecture easier to understand and reduces the computational complexity dramatically. The specific process is as follows: First, we use one Conv for the output of the data consistency block  $\mathbf{x}_{DC}$  to realize feature extraction, then GAP is applied to the Abs values of the feature maps to encode the features of the entire space on each channel as global features  $\mathbf{g}$ . After that,  $\mathbf{g}$  is fed into a two-layer FC network which contains Sigmoid at the end, so that the excitation values  $\alpha \in (0,1)$  can be obtained. The adaptive selected thresholds are  $\theta = \mathbf{g} \cdot \alpha$ . This arrangement is motivated by the fact the threshold not only needs to be positive, but also cannot be too large, thereby preventing the output features from being all zeros. For simplicity, the threshold auto-setting sub-block  $A$  can be regarded as a nonlinear function

$$\theta = A(\mathbf{x}_{DC}), \quad (S1-6)$$

The adaptive-setting thresholds  $\theta$  are used in the soft-thresholding operation  $S$ . Note that, an individual threshold is applied to each channel of the feature map. Finally, we can obtain the output spectrum  $\mathbf{x}_S$  through one Conv, which restores the number of channels of the feature map to be consistent with  $\mathbf{x}_{DC}$ . The overall learnable adaptive soft-thresholding block  $LS$  is

$$\mathbf{x}_S = LS(\mathbf{x}_{DC}, \theta). \quad (S1-7)$$

In our implementation, the architecture-related hyper-parameters of the network are listed in Table S1-2. The learnable adaptive soft-thresholding are interleaved with data consistency, to remove artifacts gradually, and finally the high-quality reconstructed spectra can be obtained.

**Table S1-2.** Architecture-related hyper-parameters of the learnable adaptive soft-thresholding block

Operations	2D NMR		3D NMR	
	Hyper-parameters	Output size	Hyper-parameters	Output size
Input	/	1×N×2	/	1×(N <sub>1</sub> ×N <sub>2</sub> )×2
1 <sup>st</sup> Conv	1×3×2, 32	1×N×32	3×3×2, 32	1×(N <sub>1</sub> ×N <sub>2</sub> )×32
1 <sup>st</sup> FC	32	1×1×32	32	1×(1×1)×32
2 <sup>nd</sup> FC	32	1×1×32	32	1×(1×1)×32
2 <sup>nd</sup> Conv (output)	1×3×32, 2	1×N×2	3×3×32, 2	1×(N <sub>1</sub> ×N <sub>2</sub> )×2

Note: Take 2D NMR for example, 1, N, 2 in the output size ‘1×N×2’ represent the number of width, height, and channels of the feature map, respectively. 1, 3, 2, 32 in the hyper-parameters of Conv ‘1×3×2, 32’ represent the size and the number of filters. 32 in the hyper-parameters of FC ‘32’ represent the number of neurons.

#### 1.2.4 Loss function and implementation details

Let  $k$  represents the  $k^{\text{th}}$  iteration (can be seen in Figure S1-1), and  $\Theta$  denotes the network trainable parameters, then the output at the  $k^{\text{th}}$  phase is  $\hat{\mathbf{x}}_k(\Theta_k, \mathbf{y})$ , and the total number of iterations is  $K$ . The overall loss function is

$$L(\Theta) = \frac{1}{KQ} \sum_{k=1}^K \sum_{q=1}^Q \left\| \mathbf{x}_{\text{ref}} - \hat{\mathbf{x}}_k^q(\Theta_k, \mathbf{y}) \right\|_2^2, \quad (\text{S1-8})$$

where  $q$  is the  $q^{\text{th}}$  ( $q=1, 2, \dots, Q$ ) FID signals, and  $\mathbf{x}_{\text{ref}}$  is the label spectrum.

In the network training phase, the number of iterations of MoDern are 10, i.e.  $K=10$ . He initialization<sup>11</sup> is used to initialize the network weights, Adam<sup>12</sup> is selected as the optimizer. The batch size is 10. The initial learning rate was set to 0.001 with an exponential decay of 0.95. Thus, the optimal parameters  $\hat{\Theta}$  are obtained by minimizing the loss function on the training dataset. The total training time are 4.7 hours and 15.8 hours for 2D and 3D NMR within 80 epochs, respectively.

We use the relative  $l_2$  norm error  $RLNE = \left\| \mathbf{x}_{\text{ref}} - \hat{\mathbf{x}} \right\|_2 / \left\| \mathbf{x}_{\text{ref}} \right\|_2$  as the quantitative criteria to evaluate the reconstruction performances in the training stage, where  $\mathbf{x}_{\text{ref}}$  is the fully sampled spectrum and  $\hat{\mathbf{x}}$  is the reconstructed spectrum. Note that, the lower  $RLNE$  represents the better performance. Figure S1-2 shows that MoDern has good convergence on both training datasets and validation datasets.

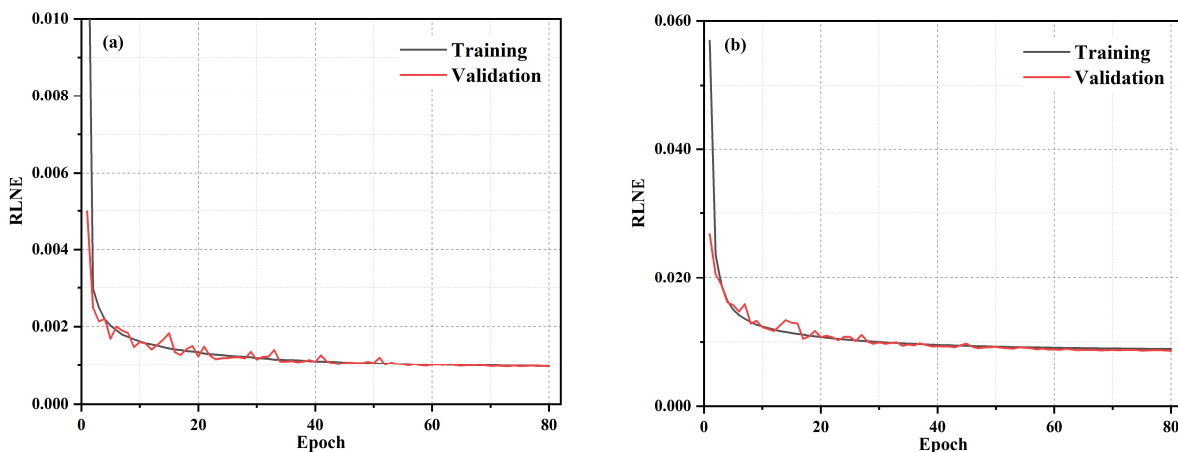


**Figure S1-2.** The training and validation *RLNE* curves of MoDern for (a) 2D NMR with 20% NUS, (b) 3D NMR with 10% NUS.

### 1.3 Reconstruction stage of the trained network and its robustness

For given undersampled FID signals  $\bar{y}$  which needs to be reconstructed, we can get the reconstructed result  $\bar{x} = f(\bar{y}, \hat{\Theta})$  through the trained network, where  $\hat{\Theta}$  and  $f(y, \hat{\Theta})$  are optimal network parameters and the optimal mapping, respectively.

Notably, MoDern is very flexible and robust, the network which is trained once under a given NUS density and spectra dimensionality (2D or 3D) can be directly applied to reconstruct the spectra with different sizes and types on different NUS density, and maintain the stable performance. So that, re-training of the network is not needed for different spectra provided that the datasets have the same dimensionality. The discussion on the mismatch between training datasets and targets can be find below, in Supplement S3.

### 1.4 Discussion on the adaptive soft-thresholding

Threshold plays an important role in the reconstruction results and exploring the proper choice of it is still of great demand and challenging. For a deep neural network with the fixed number of iterations, a too small threshold makes the majority of the artifacts remains since the effect of the  $l_1$  norm minimization is ignorable; a too large one results in serious distortion of the reconstructed spectra.

Herein, we discuss the necessity of employing adaptive soft-thresholding by comparing reconstruction results of networks with and without adaptability. The adaptive network is the proposed MoDern. The non-adaptive network is to remove the sub-block  $A$  in Figure S1-1, so that thresholds in a trained network are fixed and should not change with the characteristics of the input.

Figure S1-3 shows that, in the training stage, the adaptive network MoDern has lower reconstruction error and faster convergence speed on both training datasets and validation datasets, which implies its higher reconstruction fidelity. The above viewpoint is confirmed by the realistic NMR data. In Figure S1-4, the adaptive network MoDern surpasses the non-adaptive network in spectra quality, while being robust and can

maintain excellent performance at low NUS density.

Therefore, the adaptive soft-thresholding scheme is used to achieve more excellent and robust reconstruction results of NMR spectra.

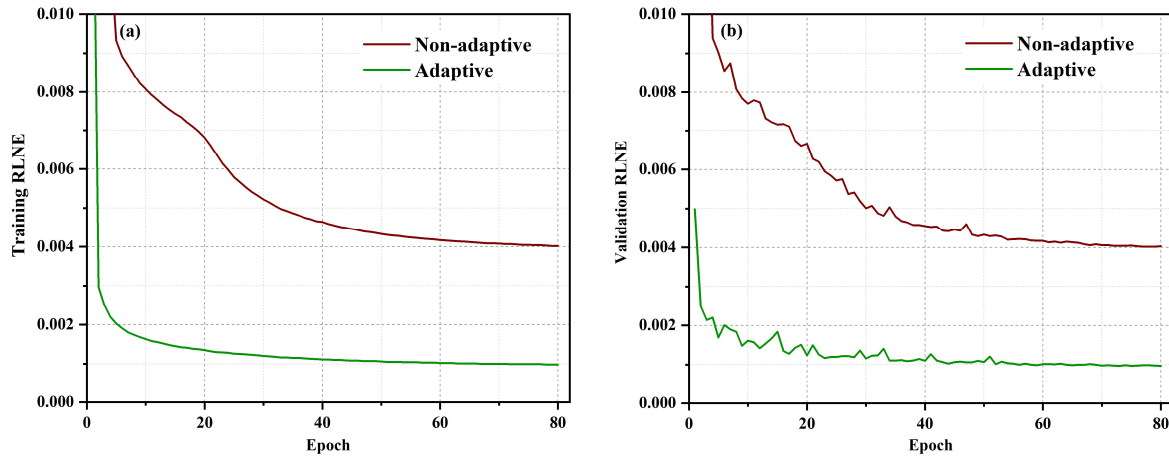


**Figure S1-3.** The *RLNE* curve of training datasets and validation datasets in the network training stage for 2D NMR. (a) The *RLNE* curve of training datasets of two network strategies. (b) The *RLNE* curve of validation datasets of two network strategies. Note: The proposed MoDern uses the ‘adaptive soft-thresholding’ strategy, due to its lowest RLNE on both two datasets.

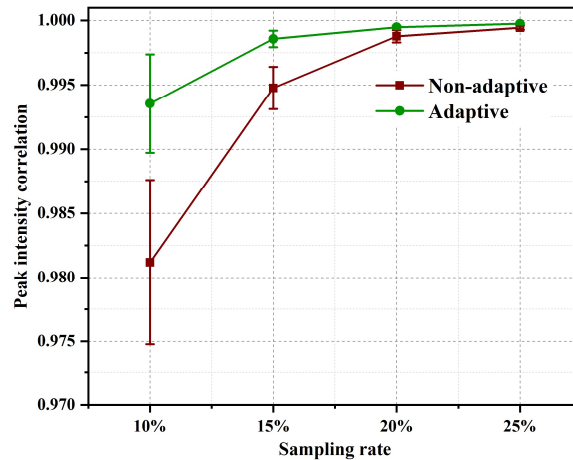


**Figure S1-4.** Peak intensity correlation obtained by the network with/without adaptive soft-thresholding under different NUS levels for 2D HSQC spectrum of cytosolic CD79b (introduced in Supplement S2). Note: The  $R^2$  denotes the square of Pearson correlation coefficient. The average and standard deviations of correlations are computed over 100 NUS trials.

## S2. More details on spectra reconstruction

The proposed MoDern will be compared with two state-of-the-art NMR spectra reconstruction methods, including a model-based optimization method (CS<sup>3</sup>) and a data-driven deep learning method (DLNMR<sup>7</sup>). And all undersampled spectra are generated according to Poisson-gap sampling<sup>8</sup>.

---

## 2.1 Details of the NMR spectra

### 2.1.1 2D spectra

The 2D  $^1\text{H}$ - $^1\text{H}$  NOESY spectrum of human ubiquitin (Figure S2-1) was acquired from ubiquitin at 298K on an 600 MHz Varian spectrometer as was described previously<sup>3</sup>. The fully sampled spectrum has  $928 \times 512$  complex points, the size of the directly detected dimension ( $^1\text{H}$ ) is followed by the size of the indirect dimension ( $^1\text{H}$ ).

The 2D  $^1\text{H}$ - $^{15}\text{N}$  HSQC spectrum of cytosolic CD79b protein (Figure S2-2) was acquired for  $300 \mu\text{M}$   $^{15}\text{N}$ - $^{13}\text{C}$  labeled sample of cytosolic CD79b in 20 mM sodium phosphate buffer at 298K on an 800 MHz Bruker spectrometer as was described previously<sup>2,7</sup>. The fully sampled spectrum has  $1024 \times 256$  complex points, the size of the directly detected dimension ( $^1\text{H}$ ) is followed by the size of the indirect dimension ( $^{15}\text{N}$ ).

The 2D  $^1\text{H}$ - $^{15}\text{N}$  HSQC spectrum of Gb1 (Figure S2-3) was acquired from GB1 at 298K on a 600 MHz Bruker spectrometer as was described previously<sup>7</sup>. The fully sampled spectrum has  $1676 \times 170$  complex points, the size of the directly detected dimension ( $^1\text{H}$ ) is followed by the size of the indirect dimension ( $^{15}\text{N}$ ).

The 2D  $^1\text{H}$ - $^{15}\text{N}$  TROSY spectrum of ubiquitin (Figure S2-4) was acquired from ubiquitin at 298K on an 800 MHz Bruker spectrometer as was described previously<sup>9</sup>. The fully sampled spectrum has  $682 \times 128$  complex points, the size of the directly detected dimension ( $^1\text{H}$ ) is followed by the size of the indirect dimension ( $^{15}\text{N}$ ).

### 2.1.2 3D spectra

The 3D HNCACB spectrum of GB1-HttNTQ7 (Figure S2-5) was acquired at 298K on an 700 MHz Bruker spectrometer as was described previously<sup>7,18</sup>. The fully sampled spectrum has  $1024 \times 90 \times 44$  complex points, the size of the directly detected dimensions ( $^1\text{H}$ ) is followed by the size of the indirect dimensions ( $^{15}\text{N}$  and  $^{13}\text{C}$ ).

The 3D HNCO spectrum of Azurin protein (Figure S2-6) was acquired on an 800 MHz Bruker spectrometer as was described previously<sup>7</sup>. The fully sampled spectrum has  $1024 \times 60 \times 60$  complex points, the size of the directly detected dimensions ( $^1\text{H}$ ) is followed by the size of the indirect dimensions ( $^{15}\text{N}$  and  $^{13}\text{C}$ ).

## 2.2 Reconstruction of 2D spectra

To demonstrate the applicability of the trained MoDern in 2D spectra, we reconstruct four spectra, including the 2D  $^1\text{H}$ - $^1\text{H}$  NOESY spectrum of human ubiquitin (Figure S2-1), the 2D  $^1\text{H}$ - $^{15}\text{N}$  HSQC spectrum of CD79b (Figure S2-2), the 2D  $^1\text{H}$ - $^{15}\text{N}$  HSQC spectrum of Gb1 (Figure S2-3), and the 2D  $^1\text{H}$ - $^{15}\text{N}$  TROSY spectrum of ubiquitin (Figure S2-4).

For the reconstruction of a high dynamic range NOESY spectrum with many weak peaks at the NUS density of 40% (Figure S2-1), MoDern and CS also can obtain high correlations ( $>0.99$ ) even on low-intensity peaks,

while DLNMR fails to handle this scenario.

For the reconstruction of three spectra with moderate dynamic range at the NUS density of 20% (Figure S2-2, S2-3, and S2-4), MoDern can obtain very high peak intensity correlation ( $>0.99$ ), and representative lineshapes of the spectra closing to the fully sampled spectra can demonstrate this. CS and DLNMR also can achieve high peak intensity correlation,  $>0.98$  and  $>0.97$ , respectively.

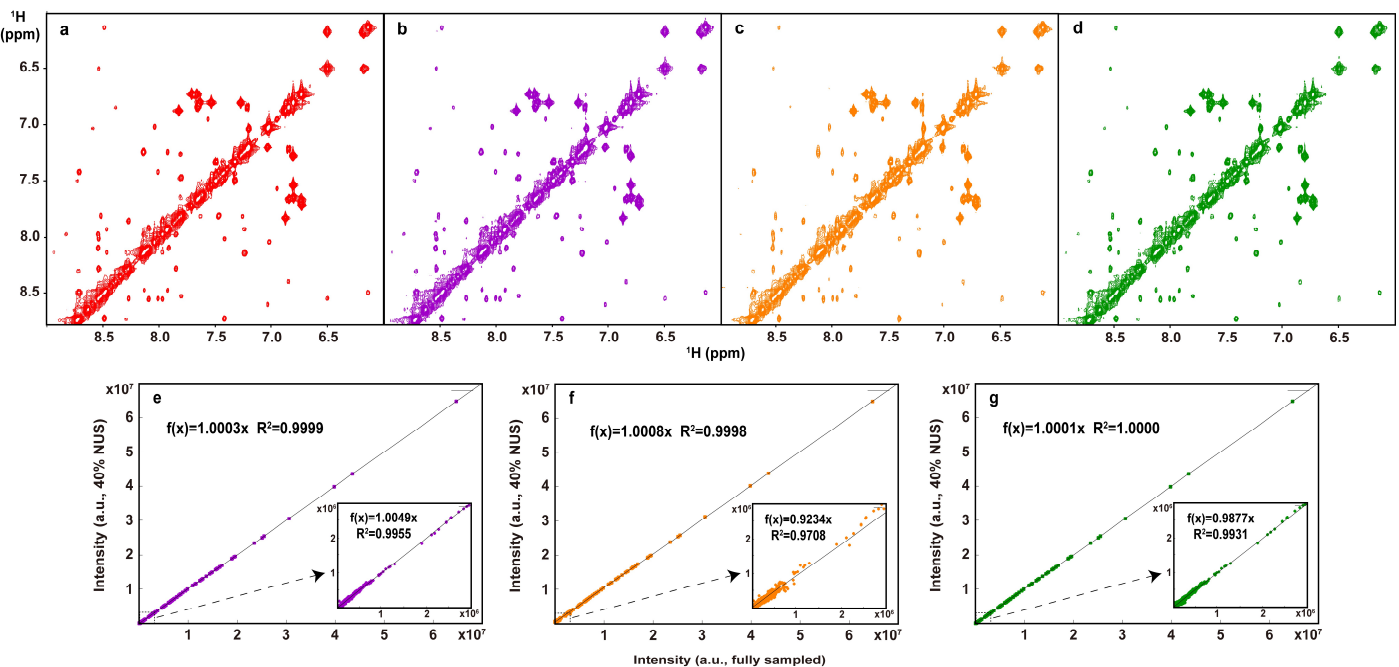


**Figure S2-1.** 2D  $^1\text{H}$ - $^1\text{H}$  NOESY spectrum of human ubiquitin. (a) The fully sampled spectrum. (b), (c) and (d) are reconstructed spectra using CS, DLNMR, and MoDern from 40% data, respectively. (e), (f), and (g) are the correlations obtained by CS, DLNMR, and MoDern, respectively. The insets of (e-g) show the peak intensity correlations of low-intensity peaks (4% of the highest intensity) obtain by CS, DLNMR, and MoDern, respectively. Note: The  $R^2$  denotes the square of Pearson correlation coefficient. The closer the value of  $R^2$  gets to 1, the stronger the correlation between the fully sampled spectra and the reconstructed spectra is.

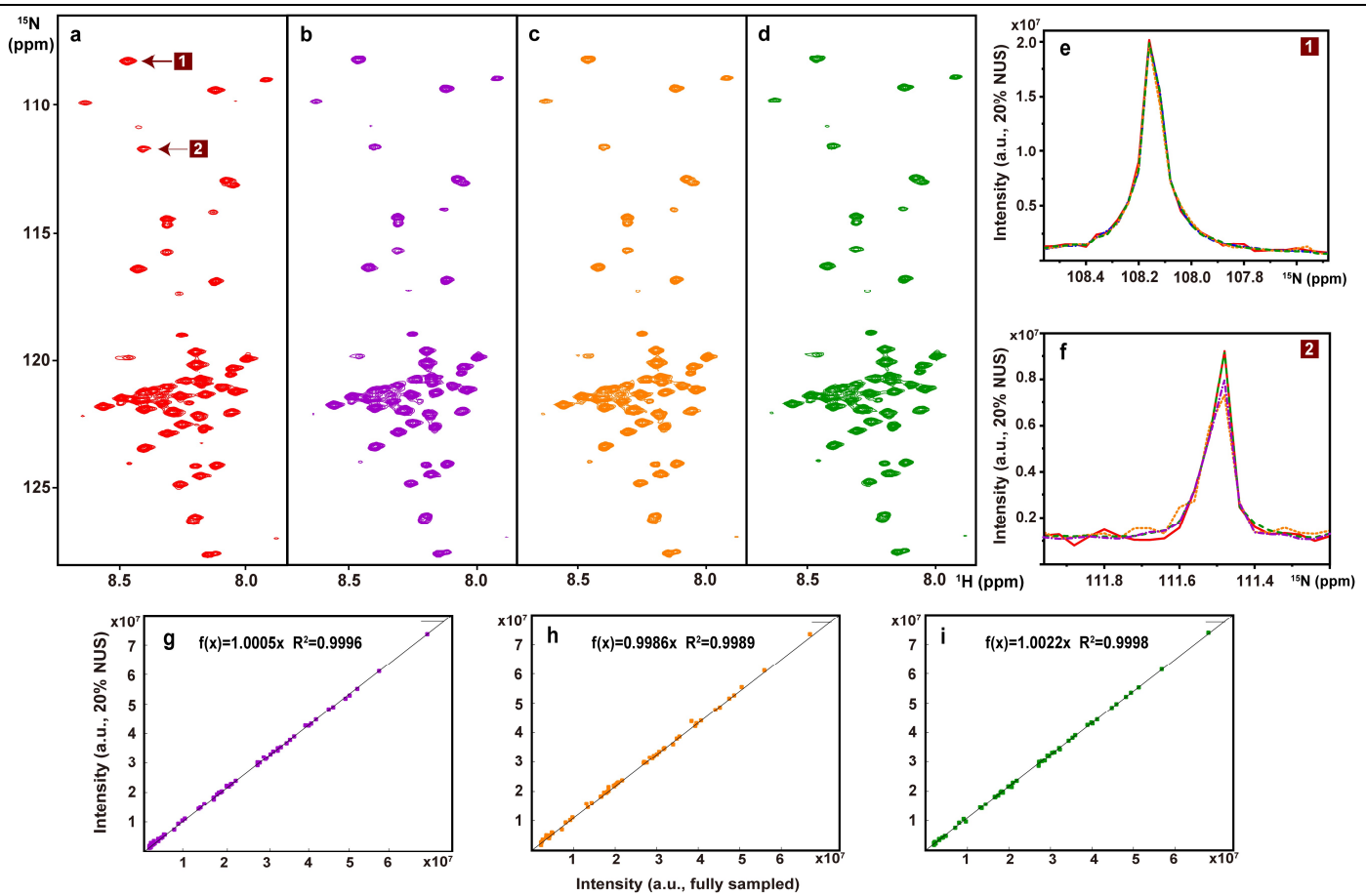


**Figure S2-2.** 2D  $^1\text{H}$ - $^{15}\text{N}$  HSQC spectrum of the cytosolic domain of CD79b protein from the B-cell receptor. (a) The fully sampled spectrum. (b), (c) and (d) are reconstructed spectra using CS, DLNMR, and MoDern from 20% data, respectively. (e) and (f) are zoomed out 1D  $^{15}\text{N}$  traces, and the red, purple, orange, and green lines represent the fully sampled spectra, CS, DLNMR, and MoDern reconstructed spectra, respectively. (g), (h), and (i) are the peak intensity correlations obtained by CS, DLNMR, and MoDern, respectively.

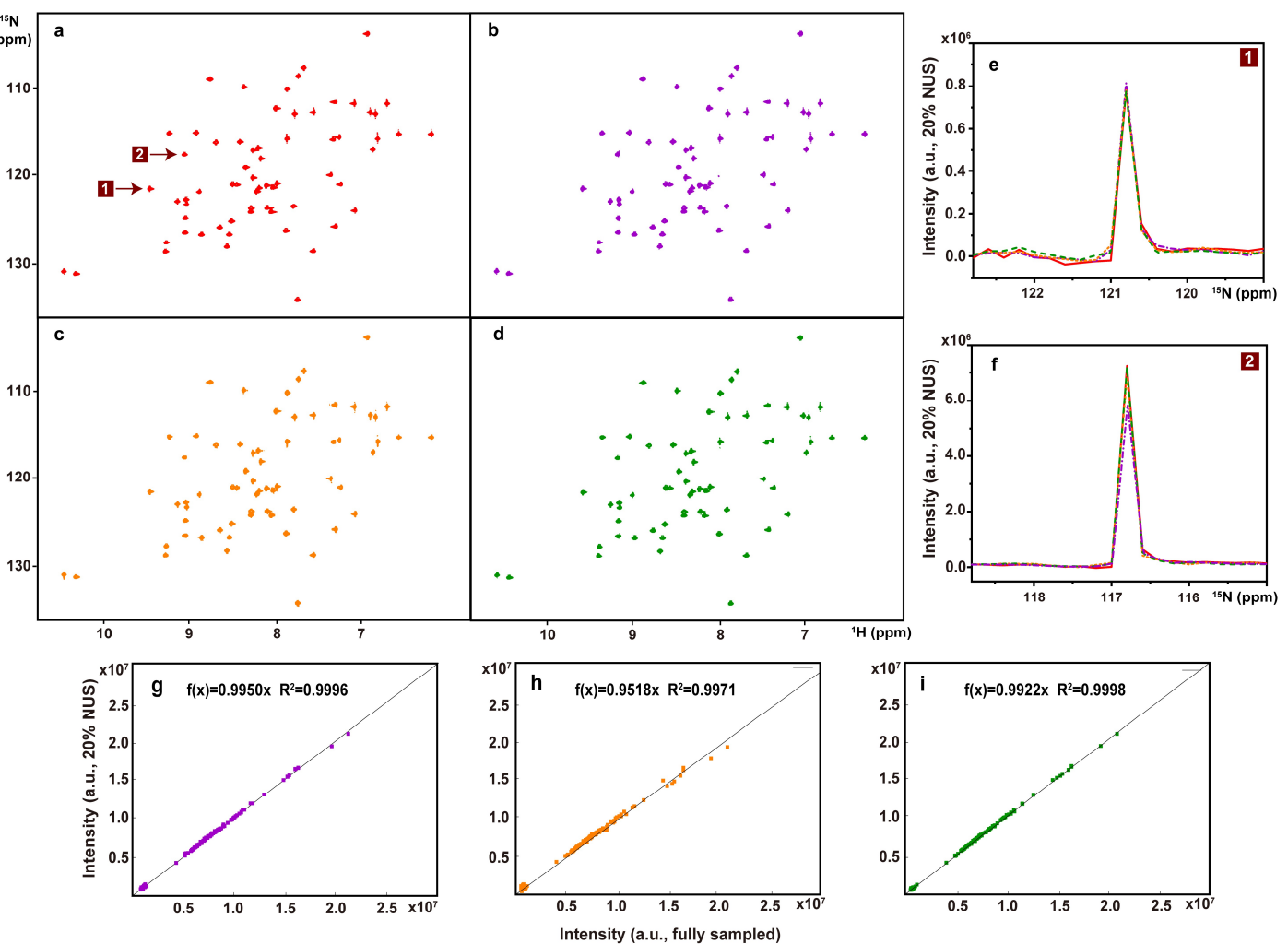


**Figure S2-3.** 2D  $^1\text{H}$ - $^{15}\text{N}$  HSQC spectrum of Gb1. (a) The fully sampled spectrum. (b), (c) and (d) are reconstructed spectra using CS, DLNMR, and MoDern from 20% data, respectively. (e) and (f) are zoomed out 1D  $^{15}\text{N}$  traces, and the red, purple, orange, and green lines represent the fully sampled spectra, CS, DLNMR, and MoDern reconstructed spectra, respectively. (g), (h), and (i) are the peak intensity correlations obtained by CS, DLNMR, and MoDern, respectively.

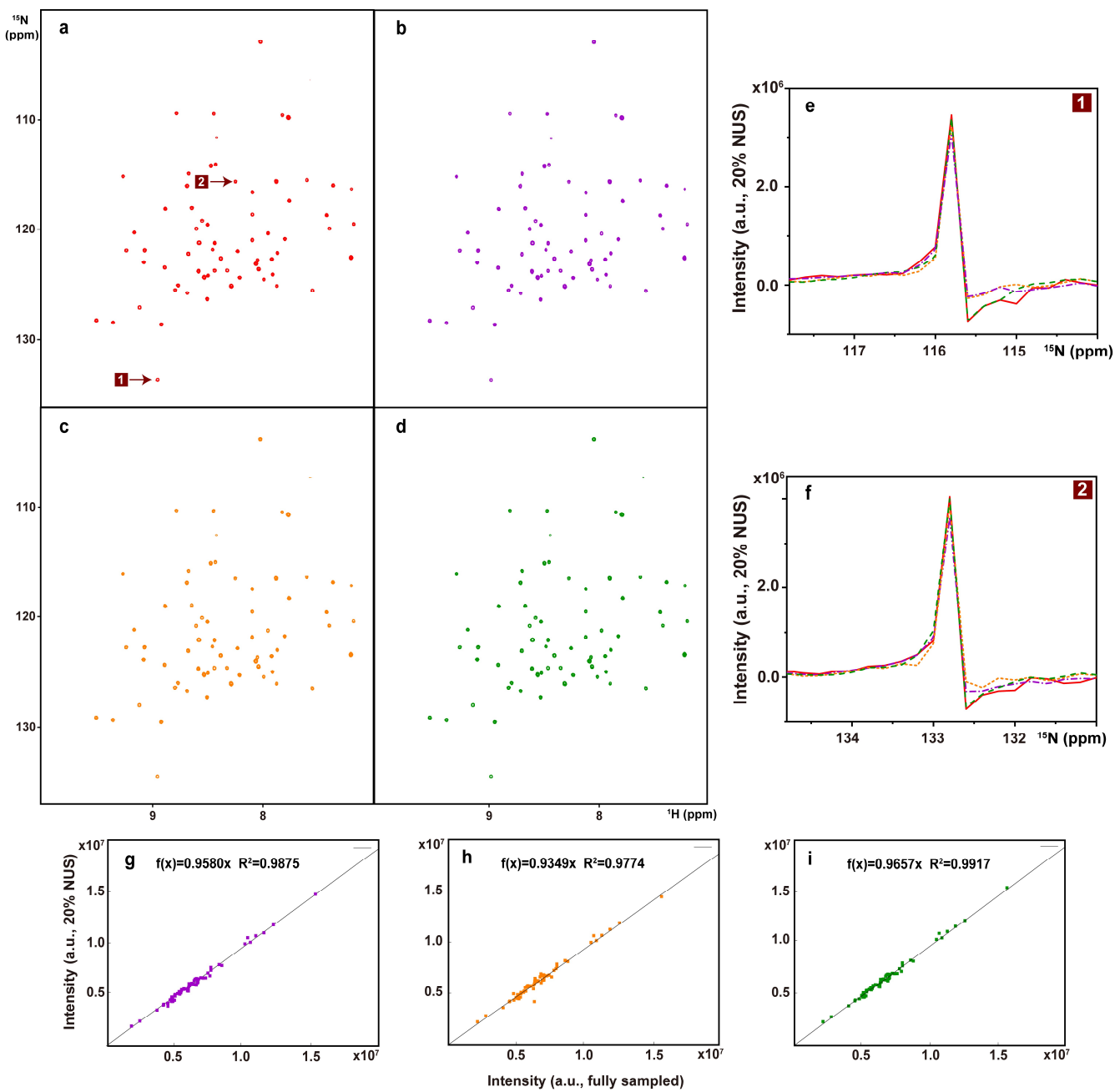


**Figure S2-4.** 2D  $^1\text{H}$ - $^{15}\text{N}$  TROSY spectrum of ubiquitin. (a) The fully sampled spectrum. (b), (c) and (d) are reconstructed spectra using CS, DLNMR, and MoDern from 20% data, respectively. (e) and (f) are zoomed out 1D  $^{15}\text{N}$  traces, and the red, purple, orange, and green lines represent the fully sampled spectra, CS, DLNMR, and MoDern reconstructed spectra, respectively. (g), (h), and (i) are the peak intensity correlations obtained by CS, DLNMR, and MoDern, respectively.

### 2.3 Reconstruction of 3D spectra

To demonstrate the applicability of the trained MoDern in 3D spectra, we reconstruct two spectra, including the 3D HNCACB spectrum of GB1-HttNTQ7 (Figure S2-5) and the 3D HNCO spectrum of Azurin protein (Figure S2-6).

For the reconstruction of two spectra, all of three methods CS, DLNMR, and MoDern can produce nice

reconstructions that are very closing to the fully sampled ones. And the peak intensity correlations of them with  $R^2 > 0.99$  shows the high fidelity of reconstruction.

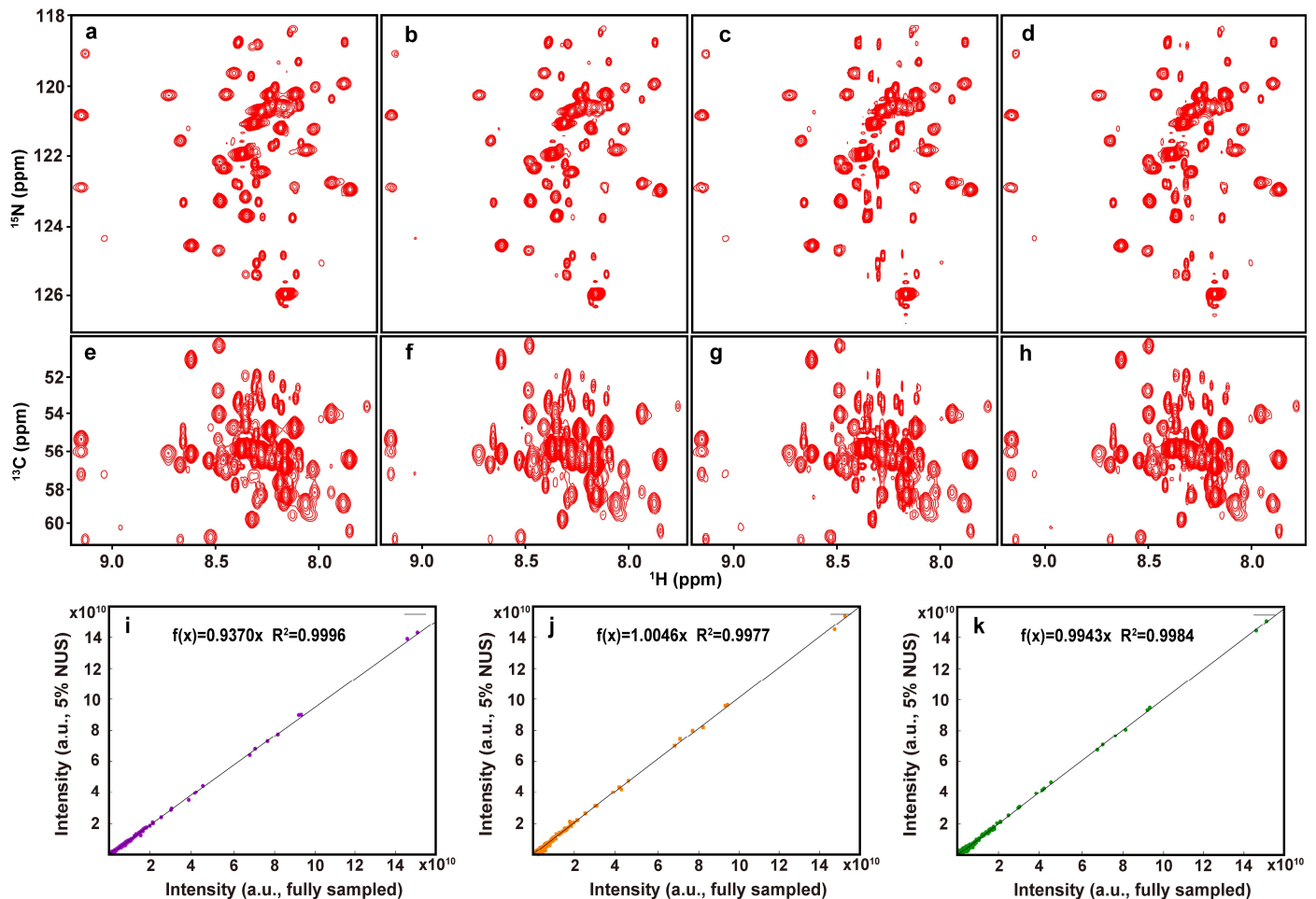


**Figure S2-5.** The sub-region of the projections on  $^1\text{H}$ - $^{15}\text{N}$  and  $^1\text{H}$ - $^{13}\text{C}$  planes of the 3D  $^1\text{H}$ - $^{15}\text{N}$  HNCACB spectrum of GB1-HttNTQ7. (a) and (e) are projections of the fully sampled spectrum. (b) and (f) are projections of the CS reconstructed spectrum. (c) and (g) are projections of the DLNMR reconstructed spectrum. (d) and (h) are projections of the MoDern reconstructed spectrum. (i), (j), and (k) are the peak intensity correlations obtained by CS, DLNMR, and MoDern, respectively. Note: 5% NUS data were acquired for reconstruction.

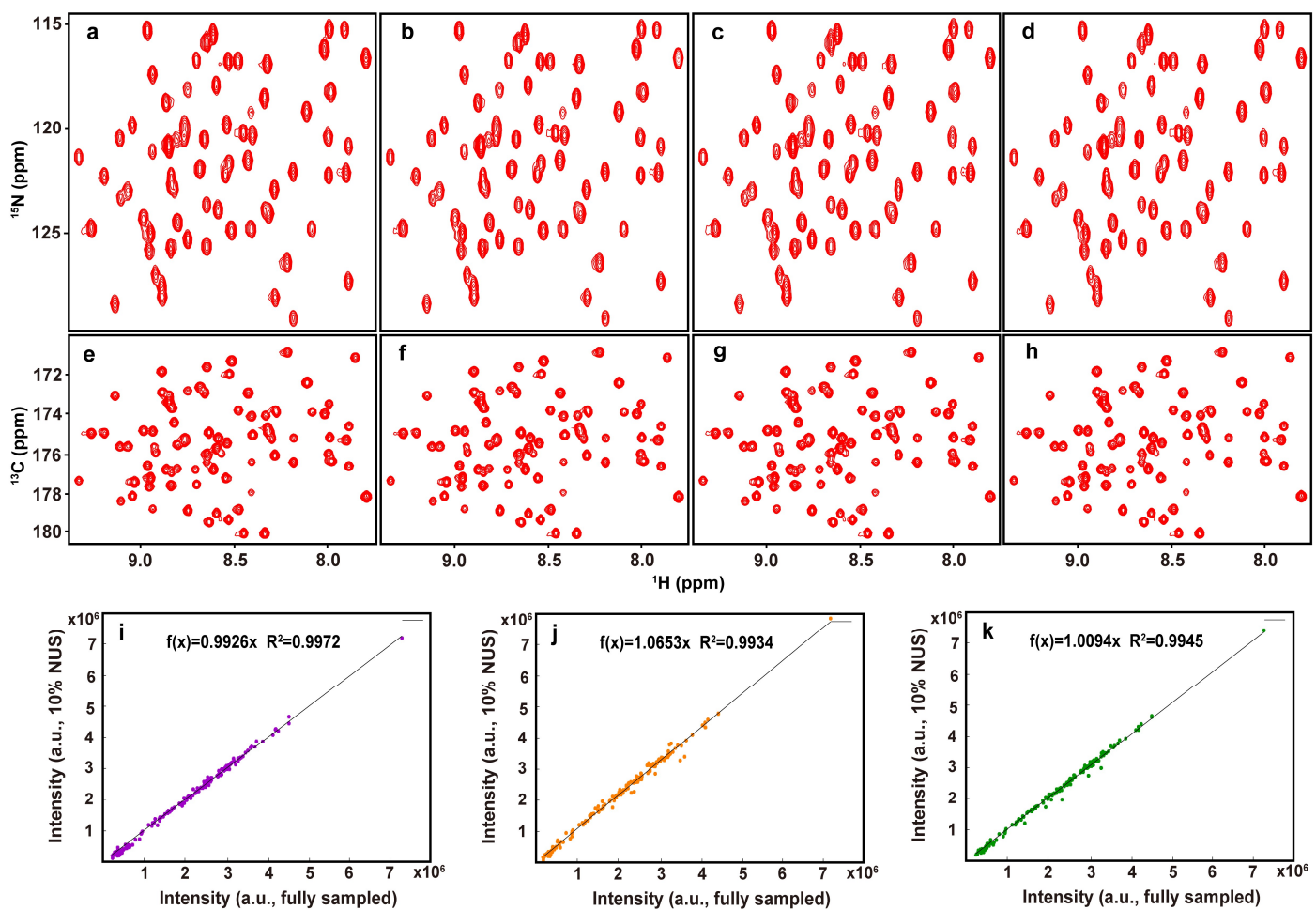


**Figure S2-6.** The sub-region of the projections on  $^1\text{H}$ - $^{15}\text{N}$  and  $^1\text{H}$ - $^{13}\text{C}$  planes of the 3D  $^1\text{H}$ - $^{15}\text{N}$  HNCO spectrum of Azurin protein. (a) and (e) are projections of the fully sampled spectrum. (b) and (f) are projections of the CS reconstructed spectrum. (c) and (g) are projections of the DLNMR reconstructed spectrum. (d) and (h) are projections of the MoDern reconstructed spectrum. (i), (j), and (k) are the peak intensity correlations obtained by CS, DLNMR, and MoDern, respectively. Note: 10% NUS data were acquired for reconstruction.

### S3. Discussion on the mismatch between training datasets and targets

In accelerated NMR spectroscopy, the existing data-driven deep learning methods<sup>7,13,14</sup> have strong dependence on training datasets, and have weak robustness and universality. Herein, we will focus on the applicability and compatibility of the proposed MoDern, to explore another important benefit of merging optimization and deep learning, in addition to the clarity of network structures and the greatly reduction of network parameters.

The strong applicability of MoDern to the spectra size and type has been detailedly demonstrated through multiple sets of reconstruction experiments in Supplement S2. In Supplement S2, for the same spectra dimensionality (2D or 3D) and NUS density, all reconstruction results are obtained by the same MoDern network, without re-training.

---

Next, we will discuss the compatibility of the proposed MoDern to different NUS densities. Among all reconstruction results in a 1D synthetic spectrum (Figure S3-1) and realistic 2D/3D NMR spectra (from Figure S3-2 to S3-6), it can be seen that the state-of-the-art data-driven deep learning method, DLNMR<sup>7</sup>, shows a significant performance decline if the NUS density of the spectrum is far from trained one. However, MoDern can maintain the stable and reliable performance, due to the introduction of reasonable sparse prior relaxing its dependence on the training dataset.

In summary, MoDern can overcome the mismatch between training datasets and real datasets, leading to work effectively in a wide range of scenarios without re-training.

### 3.1 1D synthetic spectrum

For 1D synthetic spectrum, MoDern is compared with a representative NUS NMR reconstruction methods, the data-driven deep learning method (DLNMR<sup>7</sup>). To demonstrate the applicability and compatibility of the trained MoDern, we reconstruct a synthetic spectrum with five peaks, which is introduced in Main text (Figure 2).

In Figure S3-1, MoDern can maintain the high-quality reconstruction performance even the NUS density of the spectrum is far from trained one, and lineshapes of the spectra closing to the fully sampled spectra can demonstrate this. However, DLNMR shows the significant performance decline, e.g. peak intensity distortions and artifacts, which can be seen reflected in intensity correlations of Peak 1 and reconstructed spectra.

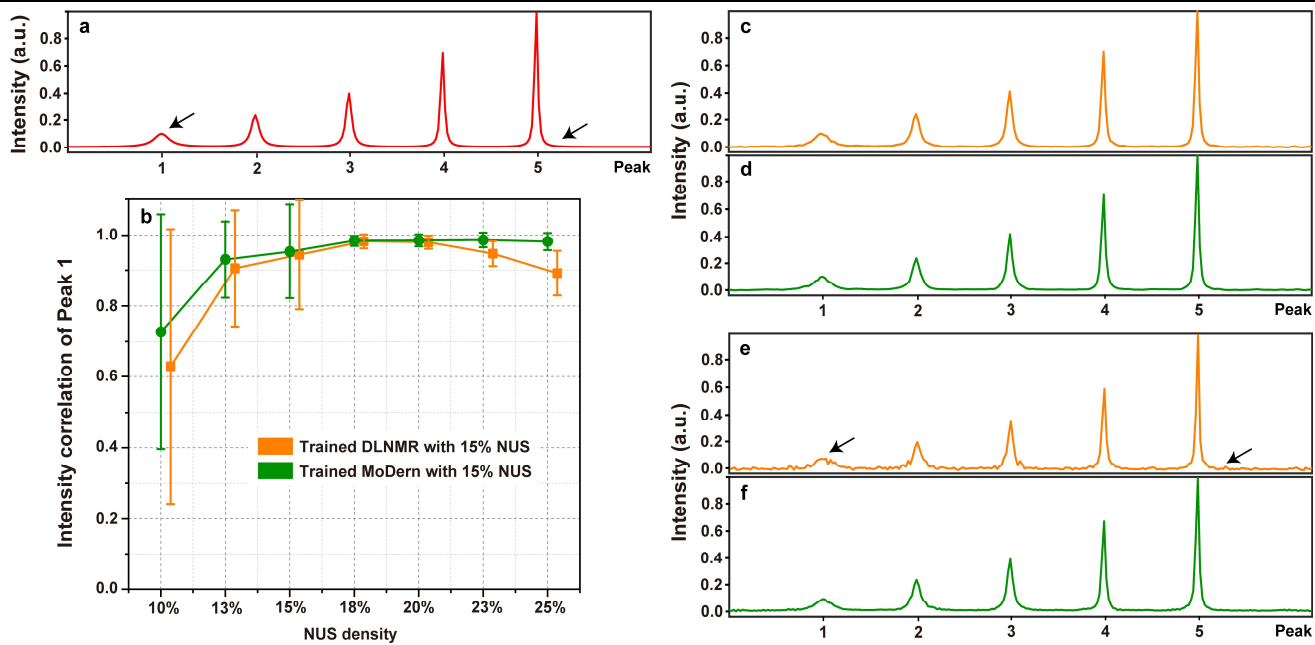


**Figure S3-1.** The reconstruction results of the trained MoDern, and the trained DLNMR from varied NUS density for 1D synthetic spectrum with five peaks. (a) The fully sampled spectrum. (b) The correlations of DLNMR and MoDern trained using 15% NUS density dataset respectively, to reconstruct the broadest Peak 1 of spectra sampled under a series of NUS densities ranging from 10% to 25%. (c) and (e) are the typical of reconstructed results of DLNMR trained using 25% and 15% NUS density datasets, respectively, to reconstruct spectra from 25% data. (d) and (f) are the typical of reconstructed results of MoDern trained using 25% and 15% NUS density datasets, respectively, to reconstruct spectra from 25% data. Note: The average and standard deviations of correlations in (b) are computed over 100 NUS trials. The peak intensity correlations of DLNMR (orange line) are shifted horizontally for clear display but the values unchanged. The intensity distortions and artifacts in (e) are marked with the black arrow.

### 3.2 2D NMR spectra

For 2D NMR spectra, MoDern is compared with a representative NUS NMR reconstruction methods, the data-driven deep learning method (DLNMR<sup>7</sup>). To demonstrate the applicability and compatibility of the trained MoDern, we reconstruct three spectra, which are introduced in Supplement S2.

For the reconstruction of two spectra with moderate dynamic range (Figure S3-2 and S3-3), MoDern can maintain the high-quality reconstruction performance even the NUS density of the spectrum is far from trained one, and very high peak intensity correlations ( $>0.999$ ) can demonstrate this. However, DLNMR shows the significant performance decline, e.g. peak intensity distortions and artifacts, which can be seen reflected in peak intensity correlations and reconstructed spectra.

For the reconstruction of a high dynamic range NOESY spectrum with many weak peaks (Figure S3-4), MoDern also have the stable and reliable performance, and can maintain the high peak intensity correlation ( $>0.99$ ) even on low-intensity peaks, while as we mentioned before, DLNMR fails to handle this scenario.

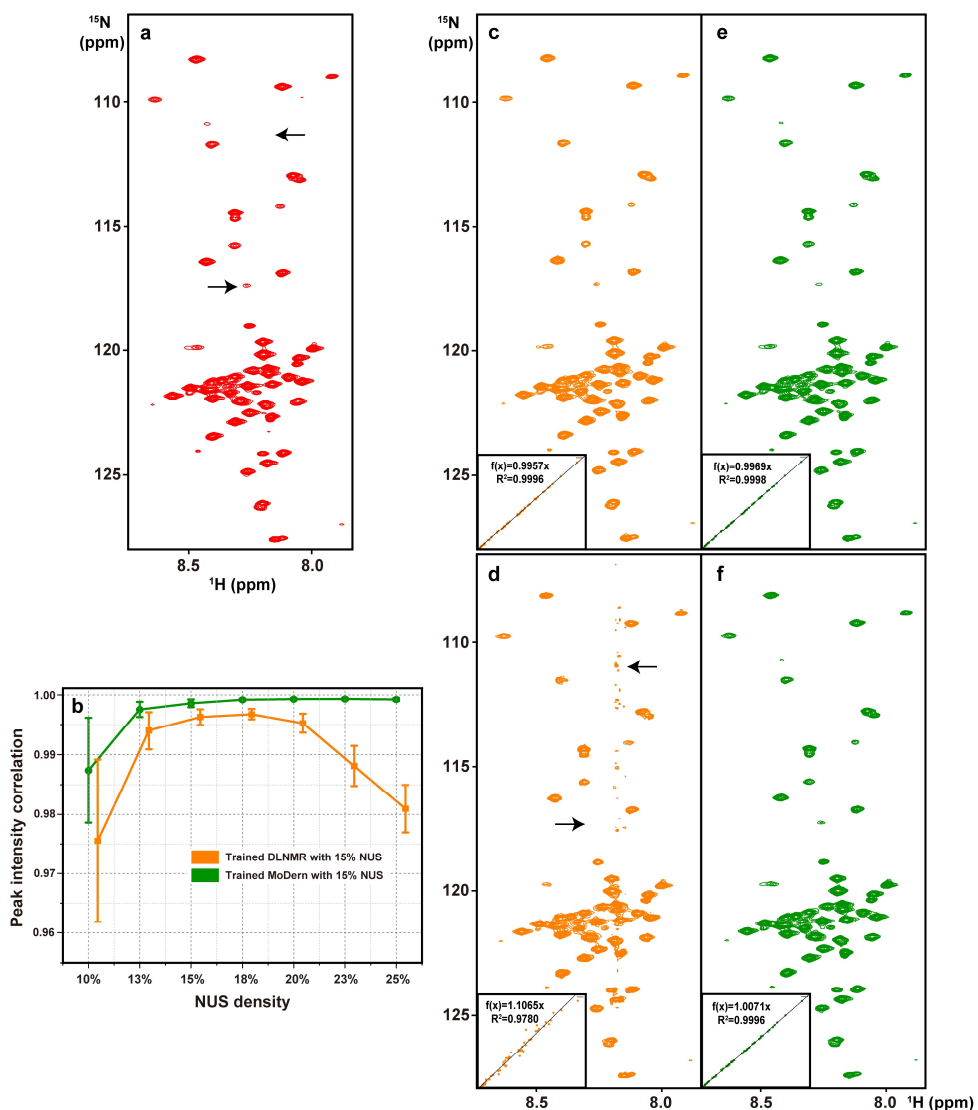


**Figure S3-2.** The reconstruction results of the trained MoDern, and the trained DLNMR from varied NUS density for 2D <sup>1</sup>H-<sup>15</sup>N HSQC spectrum of CD79b. (a) The fully sampled spectrum. (b) The correlations of DLNMR and MoDern trained using 15% NUS density dataset respectively, to reconstruct spectra sampled under a series of NUS densities ranging from 10% to 25%. (c) and (d) are the typical of reconstructed results of DLNMR trained using 25% and 15% NUS density datasets, respectively, to reconstruct spectra from 25% data. (e) and (f) are the typical of reconstructed results of MoDern trained using 25% and 15% NUS density datasets, respectively, to reconstruct spectra from 25% data. The insets of (c-f) show the peak intensity correlation between fully sampled spectrum and reconstructed spectrum. Note: The  $R^2$  denotes the square of Pearson correlation coefficient. The average and standard deviations of correlations in (b) are computed over 100 NUS trials. The peak intensity correlations of DLNMR (orange line) are shifted horizontally for clear display but the values unchanged. The intensity distortions and artifacts in (d) are marked with the black arrow.

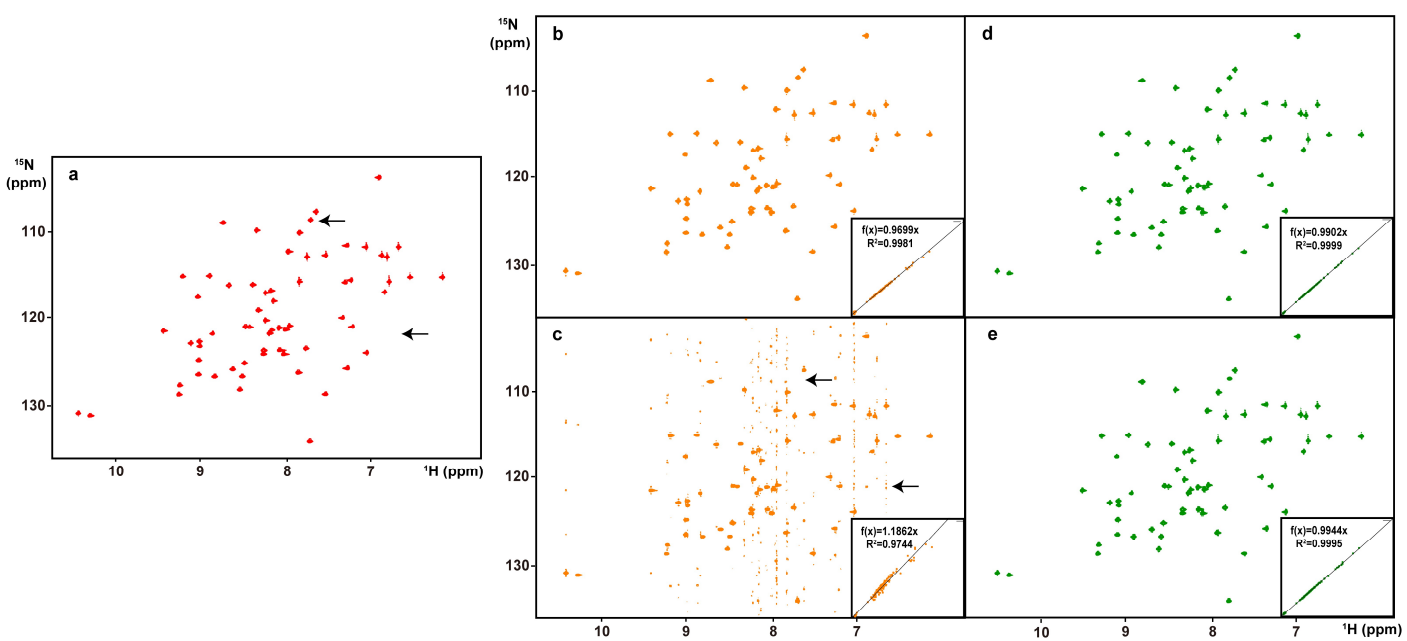


**Figure S3-3.** The reconstruction results of the trained MoDern, and the trained DLNMR from varied NUS density for 2D <sup>1</sup>H-<sup>15</sup>N HSQC spectrum of Gb1. (a) The fully sampled spectrum. (b) and (c) are the typical of reconstructed results of DLNMR trained using 25% and 15% NUS density datasets, respectively, to reconstruct spectra from 25% data. (d) and (e) are the typical of reconstructed results of MoDern trained using 25% and 15% NUS density datasets, respectively, to reconstruct spectra from 25% data. The insets of (b-e) show the peak intensity correlation between fully sampled spectrum and reconstructed spectrum. Note: The intensity distortions and artifacts in (c) are marked with the black arrow.

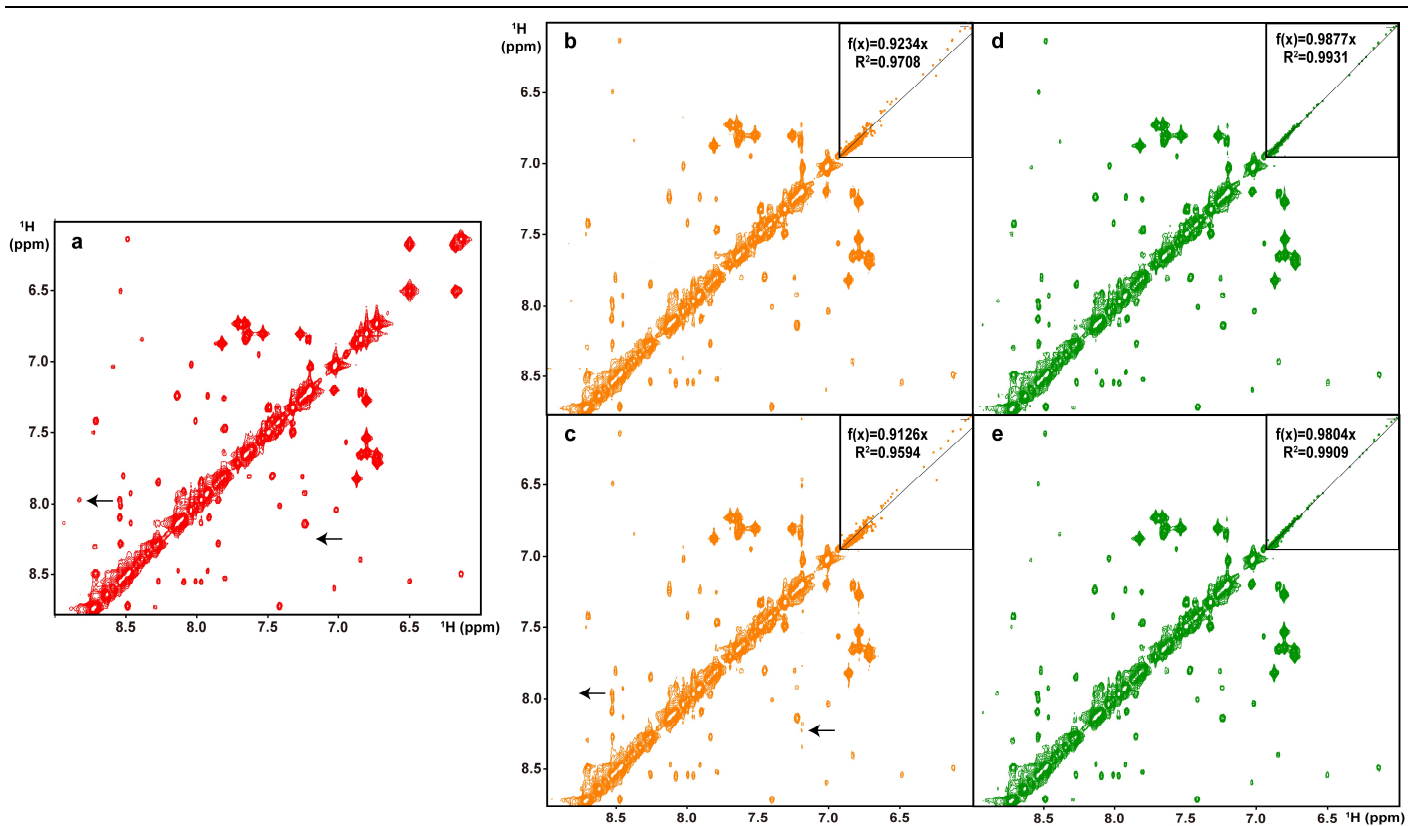


**Figure S3-4.** The reconstruction results of the trained MoDern, and the trained DLNMR from varied NUS density for 2D <sup>1</sup>H-<sup>1</sup>H NOESY spectrum of human ubiquitin. (a) The fully sampled spectrum. (b) and (c) are the typical of reconstructed results of DLNMR trained using 40% and 30% NUS density datasets, respectively, to reconstruct spectra from 40% data. (d) and (e) are the typical of reconstructed results of MoDern trained using 40% and 30% NUS density datasets, respectively, to reconstruct spectra from 40% data. The insets of (b-e) show the peak intensity correlation between fully sampled spectrum and reconstructed spectrum. Note: The intensity distortions and artifacts in (c) are marked with the black arrow.

### 3.3 3D NMR spectra

For 3D NMR spectra, MoDern is also compared with a representative NUS NMR reconstruction methods, the data-driven deep learning method (DLNMR<sup>7</sup>). To demonstrate the applicability and compatibility of the trained MoDern, we reconstruct two spectra, which are introduced in Supplement S2.

For the reconstruction of two spectra with moderate dynamic range (Figure S3-5 and S3-6), MoDern can maintain the high-quality reconstruction performance even the NUS density of the spectrum is far from trained one, and very high peak intensity correlations ( $>0.996$ ) can demonstrate this. However, DLNMR shows the performance decline, e.g. peak intensity distortions and artifacts, which can be seen reflected in reconstructed spectra.

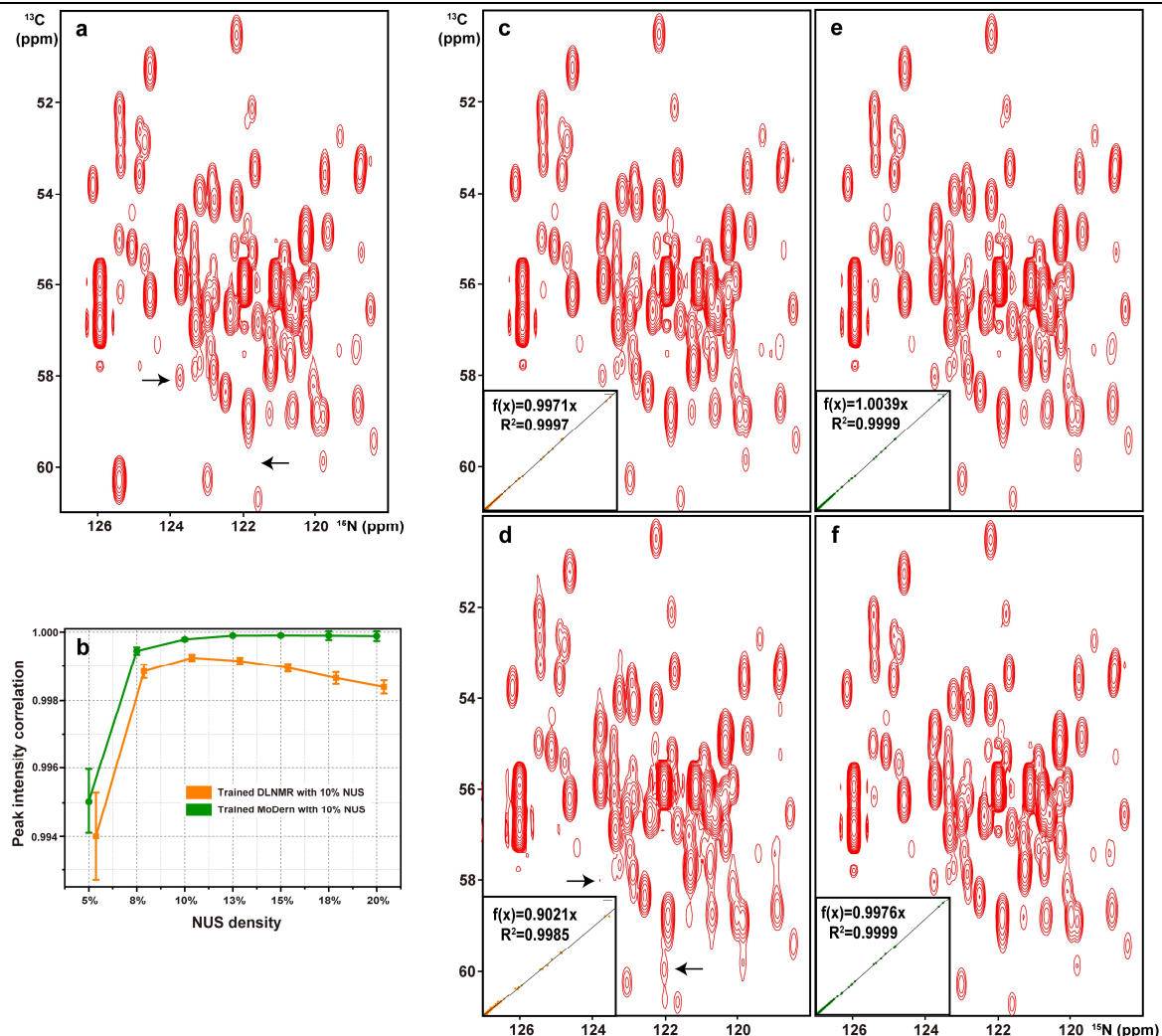


**Figure S3-5.** The reconstructed sub-region of the projections on  $^{13}\text{C}$ - $^{15}\text{N}$  planes of the trained MoDern, and the trained DLNMR from varied NUS density for 3D HNCACB spectrum of GB1-HttNTQ7. (a) The fully sampled spectrum. (b) The correlations of DLNMR and MoDern trained using 10% NUS density dataset respectively, to reconstruct spectra sampled under a series of NUS densities ranging from 5% to 20%. (c) and (d) are the typical of reconstructed results of DLNMR trained using 20% and 10% NUS density datasets, respectively, to reconstruct spectra from 20% data. (e) and (f) are the typical of reconstructed results of MoDern trained using 20% and 10% NUS density datasets, respectively, to reconstruct spectra from 20% data. The insets of (c-f) show the peak intensity correlation between fully sampled spectrum and reconstructed spectrum. Note: The average and standard deviations of correlations in (b) are computed over 50 NUS trials. The peak intensity correlations of DLNMR (orange line) are shifted horizontally for clear display but the values unchanged. The intensity distortions and artifacts in (d) are marked with the black arrow.

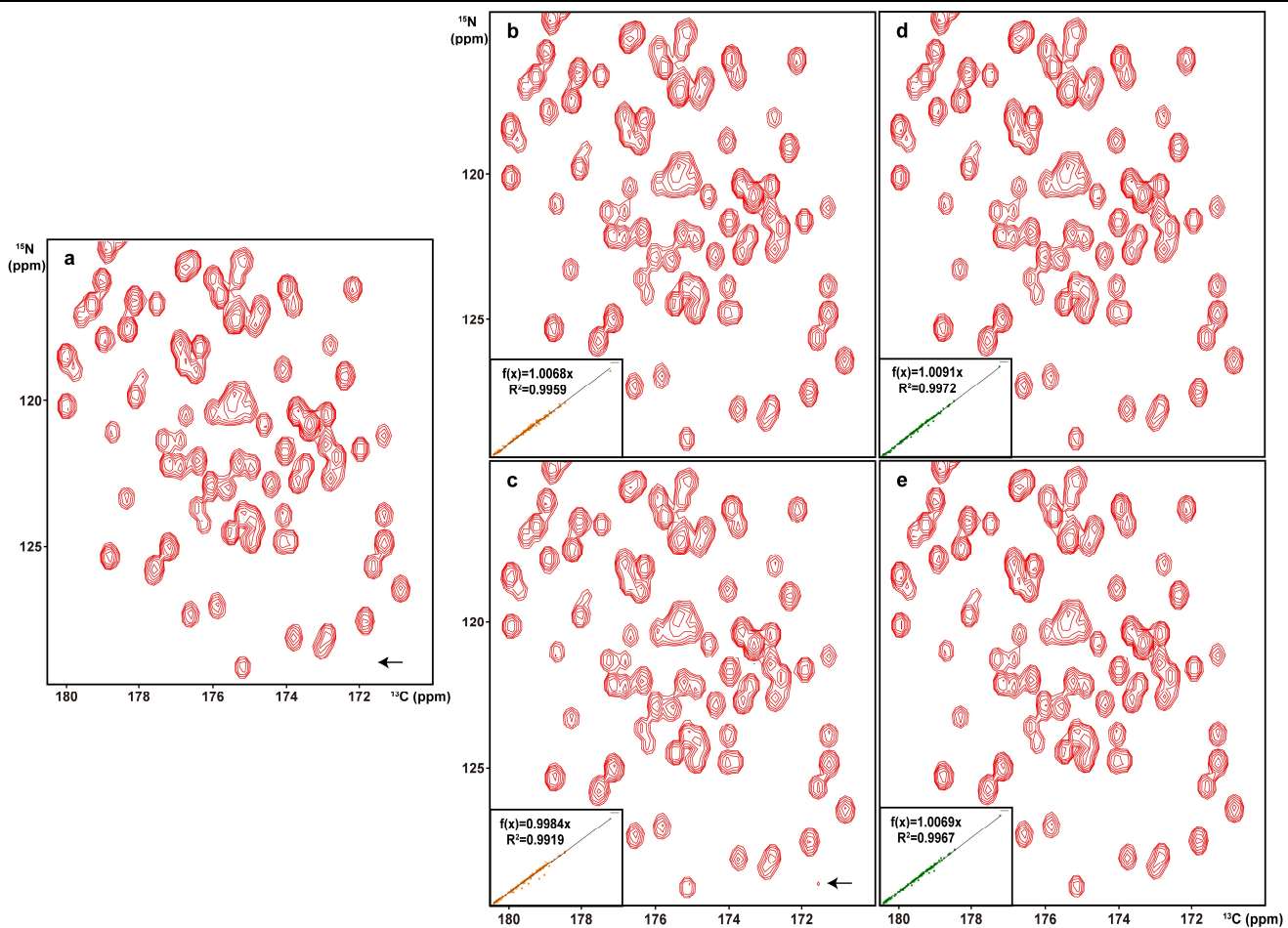


**Figure S3-6.** The reconstructed sub-region of the projections on  $^{15}\text{N}$ - $^{13}\text{C}$  planes of the trained MoDern, and the trained DLNMR from varied NUS density for 3D HNCO spectrum of Azurin. (a) The fully sampled spectrum. (b) and (c) are the typical of reconstructed results of DLNMR trained using 20% and 10% NUS density datasets, respectively, to reconstruct spectra from 20% data. (d) and (e) are the typical of reconstructed results of MoDern trained using 20% and 10% NUS density datasets, respectively, to reconstruct spectra from 20% data. The insets of (b-e) show the peak intensity correlation between fully sampled spectrum and reconstructed spectrum. The intensity distortion in (c) is marked with the black arrow.

## S4. Computational platform and time

In this section, we describe the computational platform and parameters corresponding to the results shown in the paper. Herein, the computational time of all methods is reported in Table S4-1.

All experiments implemented on a server equipped with dual Intel Xeon CPUs (2.2 GHz, 24 cores in total), 128 GB RAM, and one Nvidia Tesla K40M GPU. The proposed MoDern is performed on Python 3.6 and Tensorflow 1.14.0<sup>15</sup> as backend, as well as DLNMR<sup>7</sup>. CS<sup>3</sup> was implemented by using MATLAB 2018b with 24 threads for synthetic data and using MddNMR toolbox<sup>3</sup> with 24 threads for realistic NMR data. The CS was parallelized with aspects to the direct dimensions to maximally reduce the computation time under multiple CPU cores, and the deep learning methods were trained under one GPU.

The direct dimensions of all spectra were processed using nmrPipe<sup>16</sup>, in which the amide regions were

extracted. After reconstruction, the indirection dimensions of reconstructed data were also processed in nmrPipe. Finally, the shown spectra were analyzed using Sparky<sup>17</sup>.

CS does not require pre-training, and uses the IST algorithm with virtual echo (VE)<sup>9</sup> for optimal performance. For reconstructing synthetic data in MATLAB, its key parameters are as follows: lambda is 2.2e5, maximum iteration is 300, and tolerance is 1e-6. For reconstructing realistic NMR data in MddNMR, its key parameters are as follows: maximum iteration is 300.

DLNMR needs training before reconstruction. The network hyper-parameters are exactly the same as the original paper<sup>7</sup>. It is trained once under a given NUS density and spectra dimensionality, and then exploits for different spectra on different samples. The total training time are 10.4 hours and 43.7 hours for 2D and 3D NMR within 80 epochs, respectively.

MoDern reduces the network trainable parameters dramatically and reduces the computational complexity. It is also trained once under a given NUS density and spectra dimensionality, and then exploits for different spectra on different samples. The total training time are 3.9 hours and 15.1 hours for 2D and 3D NMR within 80 epochs, respectively, which is ca. 35% of that needed for DLNMR.

**Table S4-1.** Computational time of CS, DLNMR, and MoDern (Unit: seconds)

Spectra Type		Protein	Spectra size	Computational time		
				CS	DLNMR	MoDern
2D	HSQC	CD79b	116 × 256	0.29	0.08	<b>0.04</b>
	HSQC	Gb1	1146 × 170	3.32	0.62	<b>0.13</b>
	TROSY	Ubiquitin	512 × 128	1.22	0.17	<b>0.05</b>
	NOESY	Ubiquitin	928 × 512	1.39	0.85	<b>0.17</b>
3D	HNCACB	GB1-HttNTQ7	879 × 90 × 44	225.12	13.08	<b>3.18</b>
	HNCO	Azurin	732 × 60 × 60	44.84	9.44	<b>2.38</b>

Note: For 2D (3D) spectra, the size of the directly detected dimension is followed by the size(s) of the indirect dimension(s).

## References

1. Hoch, J. & Stern, A. *NMR data processing*. (1996).
2. Qu, X., Mayzel, M., Cai, J.-F., Chen, Z. & Orekhov, V. Accelerated NMR spectroscopy with low-rank reconstruction. *Angew. Chem. Int. Ed.* **54**, 852-854, (2015).
3. Kazimierczuk, K. & Orekhov, V. Y. Accelerated NMR spectroscopy by using compressed sensing. *Angew. Chem. Int. Ed.* **50**, 5556-5559, (2011).
4. Holland, D. J., Bostock, M. J., Gladden, L. F. & Nietlispach, D. Fast multidimensional NMR Spectroscopy using compressed sensing. *Angew. Chem. Int. Ed.* **50**, 6548-6551, (2011).
5. Shchukina, A., Kasprzak, P., Dass, R., Nowakowski, M. & Kazimierczuk, K. Pitfalls in compressed sensing reconstruction and how to avoid them. *J. Biomol. NMR* **68**, 79-98, (2017).
6. Hyberts, S. G., Milbradt, A. G., Wagner, A. B., Arthanari, H. & Wagner, G. Application of iterative soft thresholding for

---

fast reconstruction of NMR data non-uniformly sampled with multidimensional Poisson Gap scheduling. *J. Biomol. NMR* **52**, 315-327, (2012).

- 7. Qu, X. *et al.* Accelerated nuclear magnetic resonance spectroscopy with deep learning. *Angew. Chem. Int. Ed.* **59**, 10297-10300, (2020).
- 8. Hyberts, S. G., Takeuchi, K. & Wagner, G. Poisson-gap sampling and forward maximum entropy reconstruction for enhancing the resolution and sensitivity of protein NMR data. *J. Am. Chem. Soc.* **132**, 2145-2147, (2010).
- 9. Mayzel, M., Kazimierczuk, K. & Orekhov, V. Y. The causality principle in the reconstruction of sparse NMR spectra. *Chem. Commun.* **50**, 8947-8950, (2014).
- 10. Chen, D., Wang, Z., Guo, D., Orekhov, V. & Qu, X. Review and prospect: Deep learning in nuclear magnetic resonance spectroscopy. *Chem.-Eur. J.* **26**, 10391-10401, (2020).
- 11. He, K., Zhang, X., Ren, S. & Sun, J. Delving deep into rectifiers: Surpassing human-level performance on ImageNet classification. *arXiv:1502.01852*, (2015).
- 12. Kingma, D. & Ba, J. Adam: A method for stochastic optimization. *arXiv:1403.04467*, (2014).
- 13. Huang, Y., Zhao, J., Wang, Z., Guo, D. & Qu, X. Exponential signal reconstruction with deep Hankel matrix Factorization. *arXiv:2007.06246*, (2020).
- 14. Hansen, D. F. Using deep neural networks to reconstruct non-uniformly sampled NMR spectra. *J. Biomol. NMR* **73**, 577-585, (2019).
- 15. Abadi, M. *et al.* TensorFlow: Large-scale machine learning on heterogeneous distributed systems. *arXiv:1603.04467*, (2016).
- 16. Delaglio, F. *et al.* NMRPipe: A multidimensional spectral processing system based on UNIX pipes. *J. Biomol. NMR* **6**, 277-293, (1995).
- 17. Lee, W., Tonelli, M. & Markley, J. L. NMRFAM-SPARKY: Enhanced software for biomolecular NMR spectroscopy. *Bioinformatics* **31**, 1325-1327, (2015).
- 18. Kotler, S. *et al.* Probing initial transient oligomerization events facilitating Huntingtin fibril nucleation at atomic resolution by relaxation-based NMR. *Proc. Natl. Acad. Sci. U. S. A.* **116**, 3562-3571, (2019).